vehicles

MDPI

Article

System-Level Comparative Assessment of PMSM Rotor Topologies in Battery Electric Vehicles Under the WLTP Driving Cycle

Elena-Daniela Lupu [1,2,*] and Ștefan Lucian Tabacu [2]

[1] Faculty of Electrical Engineering and Computer Science, Ștefan cel Mare University of Suceava, 13 University Street, 720229 Suceava, Romania
[2] Faculty of Mechanics and Technology, National University of Science and Technology POLITEHNICA Bucharest, Pitesti University Centre, Târgu din Vale, No. 1, Arges, 110040 Piteşti, Romania; stefan.tabacu@upb.ro
* Correspondence: elena.lupu@usm.ro

Abstract

Environmental regulations, rapid technological advancements, and evolving mobility trends have led to a significant transformation of the automotive industry in recent years. The adoption of battery-electric vehicles (BEVs) has been accelerated by these developments, which are becoming increasingly efficient and widely deployed. Evaluating BEV energy consumption and performance is essential for optimizing energy efficiency, extending driving range, and developing effective control strategies under real-world operating conditions. The analysis is based on the WLTP Class 3 driving cycle, in which the vehicle operating points are projected onto the motor efficiency map to evaluate the influence of real-world operating conditions on overall propulsion efficiency. Two operating scenarios are considered: with regenerative braking and without regenerative braking. The inverter and battery are modeled using quasi-static energy-based representations to ensure system-level energetic consistency while maintaining computational efficiency. The results show that rotor topology significantly influences vehicle-level energy consumption. The dual-layer IPM configuration reduces net WLTP energy demand by approximately 9% and increases the estimated driving range from about 489 km to 535 km compared to the single-layer V-shaped configuration. Variations in rotor topology led to different efficiency distributions, which leads to systematic differences in battery energy demand and achievable driving range. The results highlight the importance of aligning traction motor design with realistic operating-point distributions rather than optimizing solely for peak efficiency or marginal improvements in regenerative braking performance.

Keywords: drive cycle simulation; efficiency map; energy consumption; PMSM; regenerative braking; range

Check for updates

Academic Editors: Nicolae Vlad Burnete, Florin Mariasiu and Calin Iclodean

Received: 7 February 2026
Revised: 5 March 2026
Accepted: 17 March 2026
Published: 20 March 2026

Copyright: © 2026 by the authors. Licensee MDPI, Basel, Switzerland. This article is an open access article distributed under the terms and conditions of the Creative Commons Attribution (CC BY) license.

1. Introduction

Electric vehicles represent one of the major strategic directions for decarbonizing road transport, with battery electric vehicles (BEVs) becoming the predominant technological solution [1–3]. Their energy performance and driving range depend not only on battery capacity but also on the architecture of the propulsion system and on how efficiently energy is converted and utilized under real driving conditions [4–6]. Within this context, the

electric motor has a central role in the vehicle energy chain, as its operating efficiency directly affects energy losses, driving range, and thermal loading [7,8].

The accelerated development of electric mobility has intensified the need for advanced energy optimization strategies in BEVs, where both the electric motor and the energy storage system critically influence overall vehicle efficiency [6,9–12]. As a result, the selection of the traction motor technology becomes a critical design decision, as it directly determines the achievable efficiency, power density, and operating characteristics of the electric propulsion system.

The traction motor represents a key component in electric vehicle powertrains, requiring an optimal balance between power density, efficiency, cost, and material availability [1,6]. Permanent magnet synchronous motors (PMSMs) are currently the most used traction motors in electric vehicle applications due to their high efficiency, high torque and power density, compact size, and excellent dynamic performance over a wide operating range [13–15]. However, their performance benefits come at the cost of a strong dependence on rare-earth permanent magnets, which significantly increases manufacturing costs and raises concerns related to material availability, price volatility, and supply chain sustainability [16–18].

In addition to PMSMs, several well-established traction motor technologies that are not dependent on permanent magnets are also employed in electric vehicle applications. Induction motors (IMs) are recognized for their robust construction, high reliability, and mature manufacturing technology, offering complete independence from rare-earth materials, although typically exhibiting lower efficiency and power density compared to PMSMs, particularly at low speeds and partial-load operating conditions [1,3]. Switched reluctance motors (SRMs) feature a simple and rugged rotor structure, inherent fault tolerance, and wide-speed-range capability; nevertheless, they usually experience increased torque ripple and acoustic noise when compared to PMSMs [1]. Electrically excited synchronous motors (EESMs) represent another established magnet-free alternative, combining synchronous operation with controllable air-gap flux via rotor field excitation, which enables improved field-weakening capability and competitive efficiency over a wide speed range, at the expense of additional excitation losses and increased system complexity [19,20].

The evaluation of energy performance for traction electric motors in battery electric vehicles (BEVs) is commonly performed using efficiency maps, which represent motor efficiency as a two-dimensional function of electromagnetic torque and rotational speed [21,22].

Unlike industrial electric motors, whose efficiency is classified under standardized IE classes, no internationally standardized efficiency classification currently exists for traction motors used in electric vehicle propulsion systems. This lack of a comprehensive efficiency classification framework is mainly due to the specific operating conditions of traction drives, which are typically inverter-fed and characterized by a wide speed range, frequent transients, and highly variable load profiles imposed by real driving conditions [10,11]. As a result, a single rated efficiency value is insufficient to accurately characterize the energy performance of traction machines. Instead, efficiency maps provide a comprehensive description of motor behavior over the entire operating envelope and enable a detailed assessment of energy consumption when coupled with specific driving cycles and vehicle operating scenarios [4,6,21]. Consequently, efficiency mapping has become a fundamental analytical tool for the comparison, optimization, and selection of traction motor technologies in modern electric vehicle applications [6,23].

In this context, the Worldwide Harmonized Light Vehicles Test Procedure (WLTP) driving cycle provides a consistent and comparable analysis framework by representing

realistic driving conditions and offering valuable insight into the relationship between vehicle load profiles and motor energy efficiency [24].

An additional measure for extending the driving range of electric vehicles is the implementation of regenerative braking, which enables the partial recovery of the vehicle's kinetic energy during deceleration phases [25–27]. In efficiency maps, this operating regime is represented in the negative-torque regions, where the conversion efficiency from mechanical to electrical energy varies significantly with speed and load [26,28]. The effectiveness of regenerative braking therefore directly affects the ability of the traction motor to operate within high-efficiency regions of the generator-mode during braking events. Consequently, both the motor design and the control strategy play an essential role in maximizing energy recuperation [28,29]. In addition, the overall regenerative braking performance depends on the coordinated interaction between the traction motor, power electronic inverter, battery management system (BMS), and mechanical braking system, which is typically implemented through braking force blending strategies [27,30].

Recent literature consistently indicates that regenerative braking can lead to a significant extension of electric vehicle driving range, with reported improvements typically ranging between approximately 8% and 25%, depending on the driving cycle, vehicle configuration, and control strategy [26,27]. Studies based on standardized driving cycles highlight this dependency, reporting average range increases of about 13% under the WLTC, approximately 16% for the NEDC, and values reaching or exceeding 30% for urban-dominated cycles [25,30]. More recent investigations further confirm these trends across different traction motor topologies and electric propulsion architectures [12,27].

In this study, a unified WLTP-based energy evaluation procedure is employed to assess the energy performance of a battery electric vehicle (BEV). By integrating longitudinal vehicle dynamics, drivetrain modeling, power electronics losses, battery behavior, and regenerative braking within a coherent simulation framework, the proposed methodology adopts a system-oriented approach for traction motor comparison.

The analysis is conducted on a BEV equipped with two permanent magnet synchronous motor (PMSM) variants while maintaining identical electrical, geometric, and thermal constraints. This ensures that the observed differences in energy consumption and driving range can be directly attributed to rotor topology. Particular emphasis is placed on the influence of the operating-point distribution generated by a realistic driving cycle on overall vehicle efficiency.

A key contribution of the work is the systematic alignment between the operating-point distribution produced by the WLTP Class 3 driving cycle and the motor efficiency maps, rather than relying solely on conventional peak-efficiency indicators. The results show that variations in efficiency distribution across the torque–speed plane may lead to measurable differences in total battery energy demand and achievable driving range over a standardized driving cycle.

Furthermore, the comparison between operating conditions with and without regenerative braking allows a detailed assessment of the interaction between traction efficiency and energy recuperation capability. The results indicate that improvements in traction efficiency do not necessarily translate into proportional gains in overall vehicle-level energy efficiency when regenerative effects are considered.

Overall, the study provides a vehicle-level perspective on rotor topology evaluation by linking electromagnetic design characteristics with energy performance indicators derived under realistic operating conditions.

The originality of the present study does not reside in the individual formulation of the governing equations, which are well established in literature, but in their coherent integration within a WLTP-consistent, operating-point-aligned comparative framework that

links vehicle longitudinal dynamics, FEM-derived motor efficiency maps, and battery-level energy analysis.

The main contributions of this paper can therefore be summarized as follows:

- The development of a WLTP-based vehicle-level evaluation framework integrating vehicle dynamics, drivetrain losses, and battery behavior;
- The systematic alignment of driving-cycle operating-point distributions with motor efficiency maps for rotor topology comparison;
- The assessment of the interaction between traction efficiency and regenerative braking effects on overall BEV energy consumption and driving range.

Future extensions of the methodology toward alternative driving cycles, advanced control strategies, and enhanced electro-thermal modeling could further broaden its applicability to next-generation electric traction systems.

2. Vehicle and Propulsion System Modeling Framework

The energy performance assessment framework employed in this work relies on the coupled simulation of the vehicle longitudinal dynamics and the functional behavior of the principal elements of the electric powertrain, namely the permanent magnet synchronous motor (PMSM), the traction inverter, and the onboard energy source. Within the adopted modeling assumptions, this integrated approach enables a consistent estimation of power flow distribution and overall energy demand under operating conditions representative of the WLTP driving cycle.

The numerical model workflow follows a sequential structure. Starting from the prescribed vehicle speed profile, the required traction forces and drivetrain operating points are derived, which subsequently allows for the evaluation of component-level electrical and mechanical loads. Based on these results, the specific energy consumption, achievable driving range, and relevant stress indicators of the electric propulsion system are quantified for the investigated operating scenarios.

2.1. Longitudinal Vehicle Dynamic Model

The longitudinal vehicle dynamics are modeled to compute the traction force required to follow the prescribed WLTP speed profile. The model accounts for aerodynamic drag, rolling resistance, inertial effects, and road load contributions. The resulting drivetrain operating points are used as inputs for the electric powertrain component models.

A backward-facing modeling strategy (Figure 1) is adopted, whereby the prescribed vehicle speed profile is used to derive the corresponding traction force and drivetrain operating conditions [1,3,4].

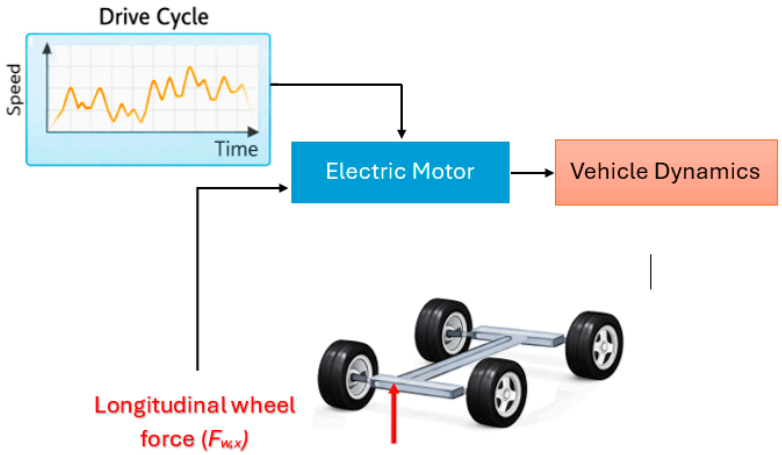


Figure 1. Backward-facing modeling strategy.

The vehicle considered in the investigation is a compact-class BEV equipped with a front-mounted PMSM-based electric powertrain, mechanically coupled to the driven wheels through a fixed-ratio transmission (final drive) and a differential.

The vehicle is modeled using longitudinal dynamics, neglecting lateral and vertical effects. The equation of motion in the longitudinal direction [4] is given by:

$$F_{w,x} = R_r + R_a + R_g + R_i \tag{1}$$

where $F_{w,x}$ denotes the total longitudinal wheel force, R_r is the rolling resistance, R_a is the aerodynamic drag, R_g is the grade resistance, and R_i is the inertial resistance. The term total longitudinal force is used to emphasize the net force required at the wheels to overcome resistive and inertial effects.

For battery electric vehicles (BEVs), the rolling resistance force represents energy losses associated with the interaction between the pneumatic tires and the road surface. It is commonly modeled as a function of the vehicle weight W and the rolling resistance coefficient f_r:

$$R_r = f_r \cdot W \cdot \cos \alpha \tag{2}$$

For passenger BEVs equipped with low rolling resistance tires, typical values of f_r range between 0.008 and 0.015 [31]. In this work, a speed-dependent formulation is adopted:

$$f_r = 0.01\left(1 + \frac{V}{160}\right) \tag{3}$$

where V is the vehicle speed in km/h. This semi-empirical expression is implemented within the longitudinal vehicle dynamics model to provide a realistic estimation of rolling resistance over the WLTP operating range.

The aerodynamic resistance R_a is given by:

$$R_a = \frac{1}{2} \cdot \rho_{air} \cdot C_D \cdot A_f \cdot v^2 \tag{4}$$

where ρ_{air} is the air density ($\rho_{air} = 1.225$ kg/m^3) corresponding to the International Standard Atmosphere conditions (dry air at 15 °C and 1 atm), commonly adopted in vehicle longitudinal dynamics modeling, C_D denotes the aerodynamic drag coefficient, A_f is the frontal projected area of the vehicle, and v is the vehicle speed relative to the ambient air.

The grade resistance R_g corresponds to the longitudinal component of the vehicle weight acting along the direction of motion and is given by:

$$R_g = W \cdot \sin(\alpha) \tag{5}$$

where α is the road inclination, typically expressed as a percentage grade $p_{\%}$. Since the WLTP cycle is defined for level-road conditions, the grade resistance term is neglected in the present analysis.

The inertial resistance R_i represents the force required to overcome the vehicle's inertia during longitudinal acceleration or deceleration and is formulated as:

$$R_i = \frac{W}{g} \cdot \gamma \cdot a \tag{6}$$

where a is the longitudinal acceleration, g is the gravitational acceleration, and γ accounts for the contribution of rotating masses to the equivalent translational inertia. For the

considered BEV with a single-speed drivetrain, γ is evaluated using a speed-dependent empirical expression:

$$\gamma = \frac{1}{1.02 - \frac{5.22}{V}} \tag{7}$$

which yields higher values at low speeds and approaches unity at high speeds. To preserve model simplicity, a constant value of $\gamma = 1.03$ is adopted.

By substituting the individual resistance components into (1) and considering WLTP level-road conditions, the required longitudinal wheel force becomes:

$$F_{w,x} = f_r \cdot W + \frac{1}{2} \cdot \rho \cdot C_D \cdot A_f \cdot v^2 + \frac{W}{g} \cdot \gamma \cdot \frac{\mathrm{d}v}{\mathrm{d}t} \tag{8}$$

Figure 2 illustrates the temporal distribution of the vehicle velocity $v(t)$, acceleration $a(t)$, and longitudinal force $F_w(t)$. The vehicle speed profile used for the determination of the longitudinal forces corresponds to the WLTP driving cycle, as detailed in Section 2.6.

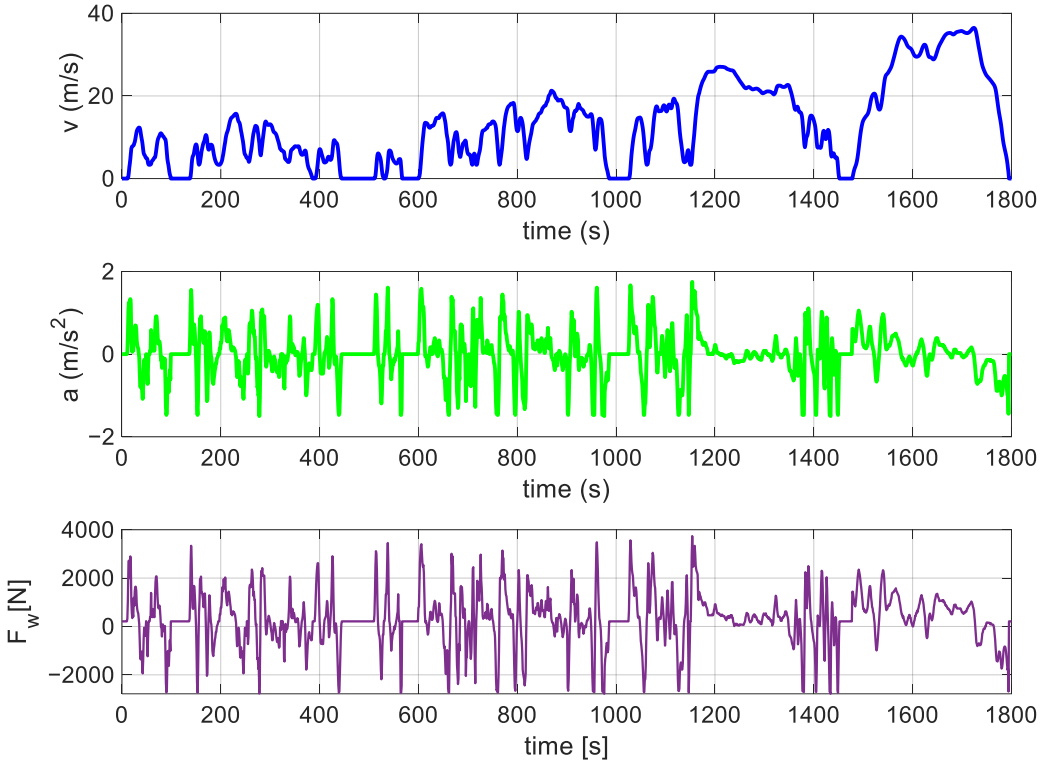


Figure 2. Vehicle speed, acceleration, and longitudinal wheel force are used as inputs for the powertrain energy analysis over the WLTP cycle.

The instantaneous mechanical power at the wheels is computed as:

$$P_w = F_{w,x} \cdot v = v\left(f_r \cdot W + \frac{1}{2} \cdot \rho \cdot C_D \cdot A_f \cdot v^2 + \frac{W}{g} \cdot \gamma \cdot \frac{\mathrm{d}v}{\mathrm{d}t}\right) \tag{9}$$

Based on the imposed speed profile, the wheel angular speed is obtained as:

$$\omega_w = \frac{v}{r_r} \tag{10}$$

where r_r is the rolling radius of the wheel.

The electric motor angular speed is obtained by applying the transmission ratio:

$$\omega_m = i_{tr} \cdot \omega_w \tag{11}$$

The mechanical torque at the wheels is determined from the power balance condition as:

$$T_w = \frac{P_w}{\omega_w} \tag{12}$$

while the torque demand at the electric motor shaft is obtained by accounting for the transmission ratio and drivetrain efficiency:

$$T_m = \frac{T_w}{i_0 \cdot \eta_{tr}} \tag{13}$$

where i_0 is the fixed transmission ratio and η_{tr} is the drivetrain efficiency.

Figure 3 presents the time evolution of the rotational speed, and mechanical torque at both the wheel and the electric motor shaft levels, confirming the validity of the adopted kinematic and dynamic conversion for mapping the WLTP driving cycle onto the torque–speed operating domain of the electric motor.

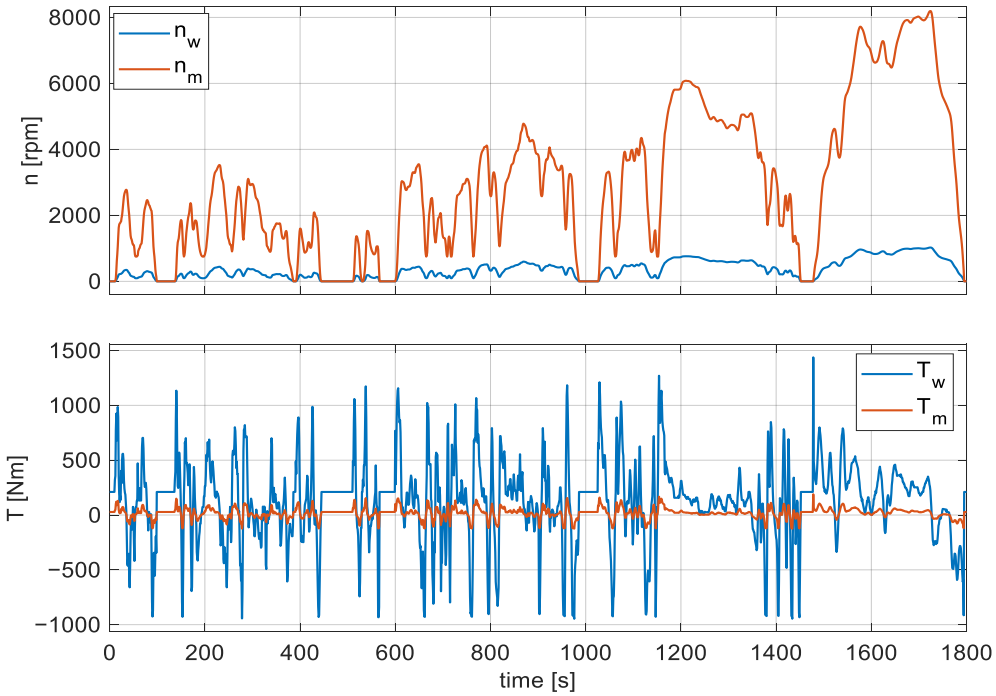


Figure 3. Rotational speed and torque response of the propulsion system over the WLTP driving cycle.

This transformation enables the direct mapping of the vehicle speed profile $v(t)$ onto the operating domain of the electric motor, defined by the (n_m, T_m) pairs, which are subsequently used to evaluate efficiency, current demand, and the overall energy performance of the propulsion system.

Figure 4 illustrates the distribution of the electric motor operating points in the torque–speed plane over the WLTP driving cycle. A high concentration of points is observed in the low- to medium-speed and moderate-torque region, corresponding to urban and extra-urban driving phases, while torque peaks occur at low speeds and the operating domain extends toward higher rotational speeds during high-velocity segments. This distribution provides the foundation for the efficiency mapping and energy consumption analysis presented in the following sections [4,5,24].

For interpretative purposes, the idealized torque–speed characteristic of the traction motor is introduced in Figure 5. This representation distinguishes the constant-torque region, limited by current capability, and the constant-power region, limited by the available inverter voltage under flux-weakening operation.

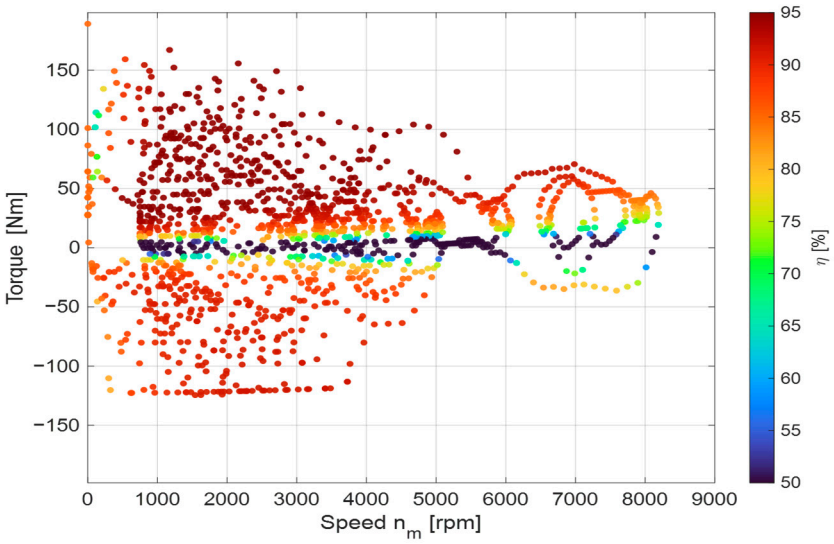


Figure 4. Operating points of the electric motor obtained from the vehicle longitudinal dynamic model over the WLTP driving cycle.

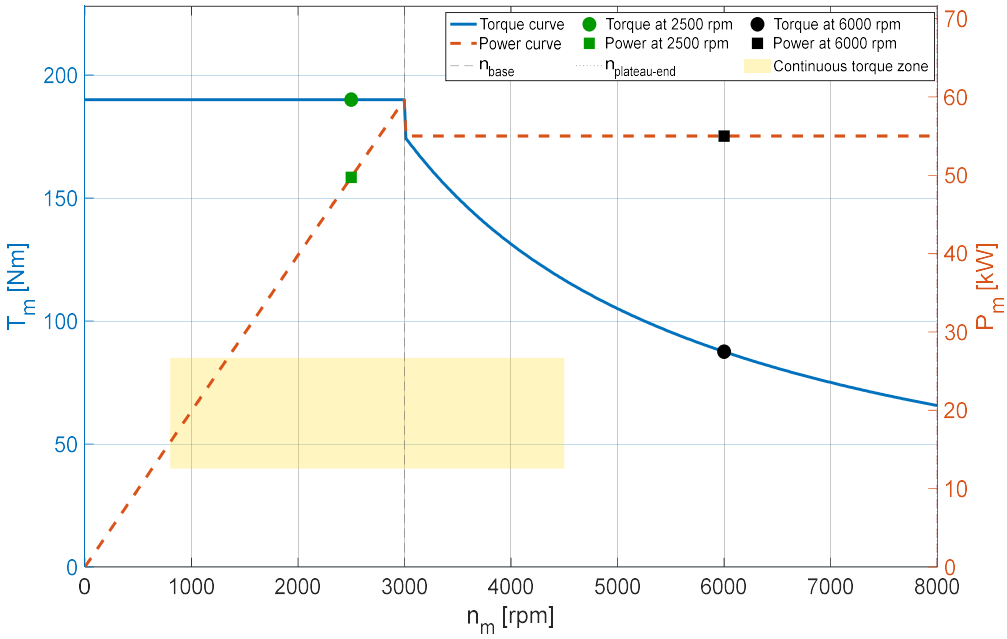


Figure 5. Idealized torque–speed characteristic of the electric traction motor.

The comparison between the actual operating points and this characteristic curve provides insight into motor loading, peak versus continuous operating conditions, and the adequacy of the selected motor and transmission parameters.

2.2. BEV Powertrain Configuration

The analyzed electric propulsion system is based on a conventional front-wheel-drive architecture with a single electric motor, which is representative of compact-class battery electric vehicles and is widely adopted in current production BEVs due to its simplicity, high efficiency, and reliability [1,3]. The electric motor is mounted on the front axle and is mechanically coupled to the driven wheels through a fixed-ratio single-speed transmission and a mechanical differential.

Figure 6 illustrates the drivetrain architecture of the BEV together with the direction of power flow during traction and the reversed torque flow during regenerative braking. During traction, electrical power is supplied by the battery and converted into mechanical

power by the inverter and the electric motor, before being transmitted to the wheels through the fixed-ratio transmission and the differential. During regenerative braking, a braking torque is generated at the wheels and transmitted back to the electric motor, allowing the recovery of kinetic energy through the inverter and the battery.

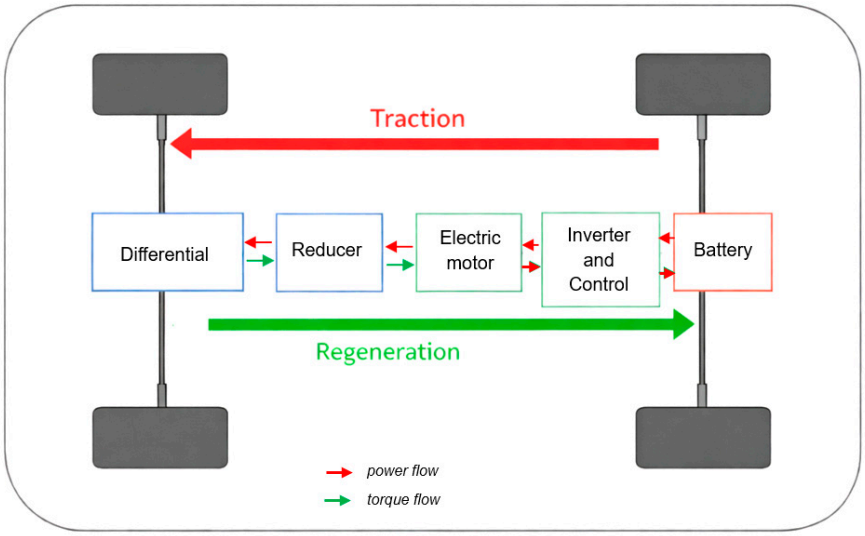


Figure 6. BEV drivetrain architecture with power and torque flow directions.

The propulsion system consists of four main components: the lithium-ion battery pack, the traction inverter, the PMSM, and the fixed-ratio mechanical transmission. The main vehicle parameters used in the simulations are summarized in Table 1 and are representative of current compact BEV platforms reported in WLTP-based studies.

Table 1. Main Parameters of the Vehicle.

Parameter	Symbol	Value	Unit
Vehicle weight	W	1950	kg
Rolling resistance coefficient	f_r	0.011	
Aerodynamic drag coefficient	C_D	0.26	
Frontal area	A_f	2.36	m^2
Air density	ρ_{air}	1.225	kg/m^3
Rotational mass inertia factor	γ	1.03	
Transmission ratio	i_0	8	
Transmission efficiency	η_{tr}	0.95	
rolling radius	r_r	0.351	m

The electrical energy stored in the battery is delivered to the inverter, which supplies the PMSM during traction operation or enables generator operation during regenerative braking, thus allowing bidirectional power flow within the propulsion system [3]. The electromagnetic torque developed by the motor is transmitted to the front wheels through the fixed-ratio transmission and the differential, providing vehicle propulsion.

The single-speed transmission configuration offers high efficiency and structural simplicity, while allowing the electric motor to operate over a wide speed range without gear shifting. As a result, a direct relationship is established between the motor operating region and the vehicle speed domain, highlighting the importance of appropriate PMSM sizing to ensure high-efficiency operation throughout the WLTP driving cycle.

2.3. PMSM Model and Efficiency Maps

The energy consumption analysis of the electric vehicle equipped with a PMSM is based on the correlation between the traction requirements imposed by standardized driving cycles and the electromagnetic characteristics of the traction motor. This approach enables the direct integration of motor efficiency maps into cycle-based energy assessments and is widely adopted in energy-oriented vehicle simulations [1,3,6].

The adopted methodology consists of three main stages:

1. Derivation of electromagnetic characteristics and efficiency maps by finite element analysis (FEM);
2. Projection of the WLTP operating points onto these maps to identify the dominant operating regions;
3. Evaluation of the vehicle energy balance, including specific energy consumption and the contribution of regenerative braking.

This framework is used to comparatively assess two PMSM traction motor configurations designed with the objective of reducing the permanent magnet mass while maintaining equivalent torque–speed performance levels, with potential benefits in terms of cost, sustainability, and supply-chain robustness for electric vehicle applications [6,8,18]. Furthermore, the impact of these design choices on the driving range and overall energy performance of the electric vehicle is assessed.

To ensure a fair comparison between the investigated rotor topologies, both PMSM variants are evaluated under identical electrical supply conditions, geometric constraints, and thermal limits. This ensures that any observed differences in efficiency, energy consumption, or driving range originate solely from the rotor topology.

To satisfy the torque and power requirements derived from the vehicle longitudinal dynamic model, two PMSM designs are considered. Both configurations share an identical stator geometry and overall dimensional envelope, while differing exclusively in the rotor magnetic topology. The constructive and electromagnetic constraints adopted for the PMSM design are summarized in Table 2.

Table 2. Main design and electromagnetic constraints of the traction PMSM.

Parameter	Symbol	Value/Specification	Remarks
Minimum continuous mechanical power at the shaft	P_{mec}	$\geq$50 kW	minimum value required for compact-class BEV applications
Maximum current density (RMS)	J_{max}	10–15 A/mm^2	limited by thermal and cooling constraints
Number of stator slots	Q	48	enables an optimal magnetic field distribution and harmonic reduction
Stator winding configuration	–	Three-phase hairpin winding	favorable for high efficiency at high loads and low-to-medium speeds
Number of rotor poles	2p	8	typical configuration for BEV traction motors
Cooling system	–	liquid cooling	required for high current densities and WLTP operating conditions

The geometric dimensions were defined as design inputs, following the imposition of the electromagnetic and constructive constraints outlined previously. The stator outer and inner diameters are 250 mm and 170 mm, respectively, while the rotor outer diameter and shaft diameter are 168.5 mm and 65 mm. The active axial length is set to 160 mm. These dimensions are representative of traction motors for compact-class BEVs and allow

continuous mechanical power levels of 70–90 kW, with peak power values of 100–120 kW over limited time intervals of 30–60 s.

Both designs employ interior permanent magnet (IPM) rotor configurations as presented in Figure 7 using NdFeB magnets doped with Dy/Tb and are equipped with three-phase hairpin windings, which are commonly adopted in automotive traction motors due to their high slot fill factor, favorable thermal behavior, and suitability for high-current operation [8,21]. Liquid cooling and a Class H insulation system are assumed to ensure reliable operation under WLTP duty conditions.

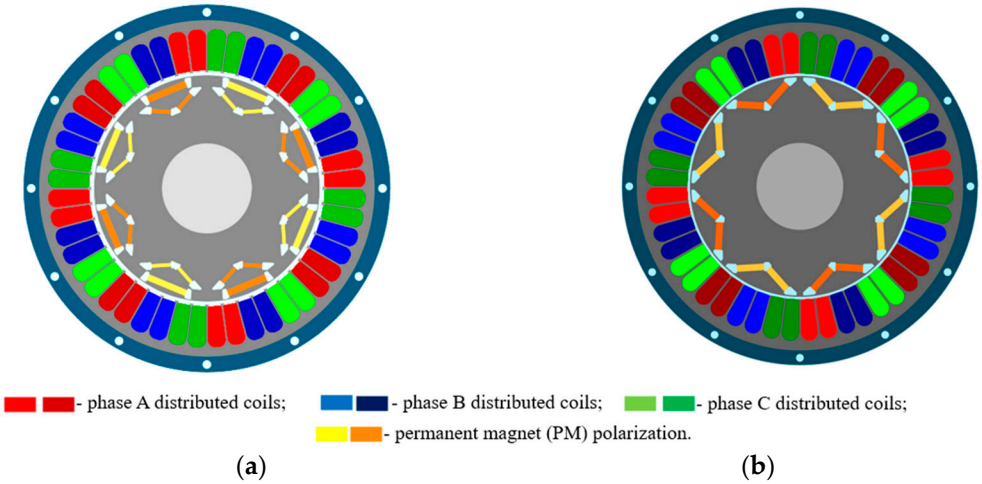


Figure 7. PMSM design for BEV traction: (**a**) M1: dual-layer IPM rotor; (**b**) M2: single-layer V-shaped IPM rotor.

The two PMSM rotor configurations investigated in this study are denoted as M1 and M2. The design parameters introduced in this section serve exclusively to define and differentiate the two topologies, while their electromagnetic performance and energy-related results are presented separately in Section 3.

The M1 rotor adopts a dual-layer IPM configuration, with two permanent magnet layers embedded in each rotor pole. This topology enhances the air-gap flux density and increases the contribution of permanent magnet torque, leading to improved torque capability at low speeds and increased resistance to demagnetization under high-load conditions, as reported for multilayer IPM designs [16,18]. However, this solution requires a larger volume of permanent magnetic material and involves higher manufacturing complexity.

In contrast, the M2 rotor employs a single-layer V-shaped IPM arrangement, which is widely adopted in production electric vehicles. This configuration provides a balanced contribution of permanent magnet torque and reluctance torque, enabling efficient operation over a wider speed range and improved field-weakening capability [16–18]. The V-shaped configuration facilitates extended high-speed operation while reducing the required permanent magnet mass, offering a favorable compromise between cost, efficiency, and performance.

By maintaining identical stator geometry and winding characteristics, the influence of the rotor magnetic topology on torque production, efficiency distribution, and operating range can be isolated and quantitatively evaluated by FEM.

The geometric parameters used to describe the embedded permanent magnets are defined in Figure 8, where only symbolic notations are indicated. In this figure, W_M and T_M denote the tangential width and radial thickness of the magnets, respectively, α is the V-angle, t_{tip} and t_{apex} represent the embedding depths at the magnet tip and at the V-apex, and r_{PM2} indicates the radial position of the inner magnet layer.

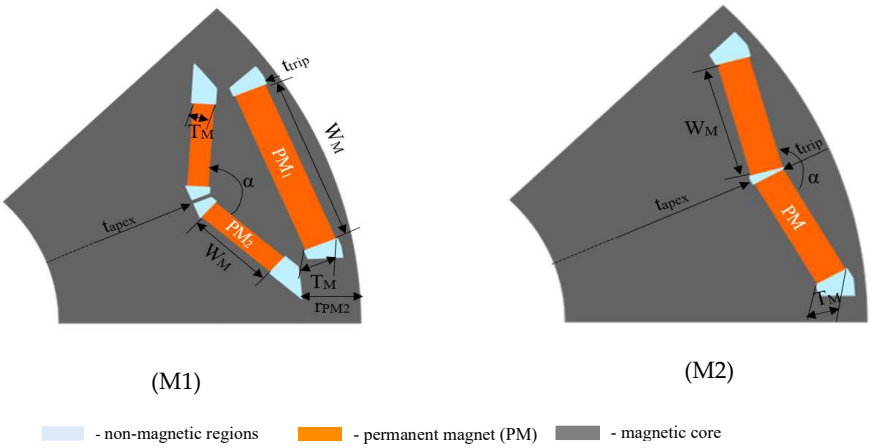


Figure 8. Technical specifications of the interior embedded permanent magnets of the traction.

The corresponding numerical values for each configuration are reported in Table 3. To reduce parasitic effects, an axial skew of 3.94° mechanical (approximately 7.9° electrical), corresponding to one stator slot pitch for an eight-pole rotor, is applied to the rotor magnets in both designs. This measure mitigates cogging torque and torque ripple, contributing to smoother operation and reduced acoustic noise, particularly at low speeds [8,14].

Table 3. Definition of the geometric parameters of the interior permanent magnets.

Parameter	Symbol	M1 (PM1 + PM2)	M2 (PM)
Tangential magnet width	W_M	28.0/15.0 mm	22.0 mm
Radial magnet thickness	T_M	4.0/2.6 mm	6.0 mm
V-angle	α	124°	124°
Embedding depth at tip	t_{tip}	2.5	15.0 mm
Embedding depth at apex	t_{apex}	21.0 mm	2.0 mm
Radial position of PM2	r_{PM2}	17.6 mm	–

Although the total motor masses of the two configurations are comparable, relevant differences arise at the rotor level due to the redistribution of active materials between permanent magnets and laminated ferromagnetic steel. These differences are summarized in Table 4.

Table 4. Comparative distribution of active materials and rotor inertia for the investigated PMSM configurations.

Characteristic	M1	M2
Total motor mass	76.15 kg	76.39 kg
Total rotor mass	34.07 kg	34.03 kg
Permanent magnet mass	3.07 kg	2.53 kg (−17% NdFeB)
Rotor inertia J_r	8.865×10^{-2} kg·m^2	8.999×10^{-2} kg·m^2

The M1 configuration employs a higher amount of NdFeB permanent magnets, resulting in an increased mass of active magnetic material at the rotor level. This design choice favors higher electromagnetic torque capability at low and medium speeds, at the expense of increased material cost and reduced sustainability.

In contrast, the M2 configuration achieves a reduction of approximately 17% in permanent magnet mass by compensating with a larger volume of laminated ferromagnetic

material. This solution leads to a more advantageous trade-off between performance, material cost, and resource availability.

The rotor inertia values of the two configurations differ only marginally, with M2 exhibiting slightly higher inertia. This variation is sufficiently small so that it is not expected to significantly affect the longitudinal dynamic behavior of the investigated electric vehicle.

A physically based evaluation of the inertia coefficient, accounting for rotor inertia and drivetrain parameters, is given by:

$$\gamma = 1 + \frac{J_r \cdot i_0^2}{W \cdot r_r^2}. \tag{14}$$

For the investigated motor configurations, this expression leads to $\gamma \approx 1.024$, which closely matches the value obtained from the empirical speed-dependent formulation adopted in the vehicle dynamic model.

The obtained values for the total motor mass and rotor component masses fall within realistic ranges for traction motors used in compact electric vehicles, thereby confirming the dimensional and constructive plausibility of the two proposed PMSM configurations and providing a coherent basis for the subsequent electromagnetic analysis.

To ensure methodological transparency and reproducibility, this subsection provides a detailed description of the finite element modeling procedure used to generate the PMSM electromagnetic performance maps, including the simulation environment, modeling assumptions, meshing strategy, material properties, and boundary conditions.

The electromagnetic behavior of the two PMSM traction motor configurations (M1 and M2) was investigated using a two-dimensional finite element model implemented in Altair FluxMotor Advanced, which is specifically dedicated to the design and electromagnetic analysis of rotating electrical machines and is based on a 2D magneto-quasi-static formulation. The problem was formulated using the magnetic vector potential A, derived from Maxwell's equations under magneto-quasi-static conditions. The governing equation solved over the computational domain is:

$$\nabla \times (\upsilon \cdot \nabla \times \mathrm{A}) = J + \nabla \times M \tag{15}$$

where A denotes the magnetic vector potential, ν is the magnetic reluctivity, J represents the impressed current density in the stator windings, and M denotes the magnetization vector of the permanent magnets. Nonlinear magnetic material behavior was accounted for by means of B–H characteristics for the ferromagnetic regions.

The machine geometries were discretized using second-order triangular finite elements with local mesh refinement in the air-gap region to accurately capture the high magnetic field gradients. A mesh refinement verification was conducted to ensure numerical convergence of the electromagnetic torque and loss calculations, indicating that further mesh densification produces negligible variations in the computed results.

Accordingly, the resulting nonlinear system of equations was solved using an iterative Newton–Raphson scheme combined with sparse matrix solvers. The numerical solution accuracy was verified through mesh refinement and convergence checks to ensure stable evaluation of torque and electromagnetic losses. Steady-state electromagnetic solutions were computed for discrete operating points corresponding to different current and speed levels, enabling the generation of torque–speed, power–speed, efficiency, and loss maps for both motor configurations. The electromagnetic torque was evaluated using Maxwell stress tensor and co-energy methods, as implemented in the Flux solver. The computed results were subsequently employed for the derivation of efficiency maps and loss distributions for the electromagnetic evaluation, operating conditions relevant to the investigated BEV

application were defined. A line voltage of 400 V was assumed, consistent with the battery and inverter architecture, together with a nominal current of 250 A and a maximum rotational speed of 14,000 rpm, representative of traction applications in the C-segment. The adopted control strategy is Maximum Torque Per Voltage (MTPV), which allows extension of the operating range beyond the base speed by optimally exploiting the inverter voltage limit.

Since high-speed operation has a direct impact on electromagnetic losses and thermal behavior, the simulations were carried out assuming a reference winding temperature of 150 °C. This value remains below the admissible limit of the Class H insulation system (180 °C), ensuring an adequate thermal safety margin under driving-cycle conditions.

The FEM simulations yielded efficiency maps, phase current distributions, electromagnetic loss maps, and characteristic torque–speed and power–speed curves for both motor configurations, as illustrated in Figure 9 Such FEM-based performance mapping is a well-established approach for traction motor evaluation and energy simulation of electric vehicles [6,21–23]. The resulting efficiency and loss maps constitute the input data for the vehicle-level WLTP energy simulations presented in the following sections.

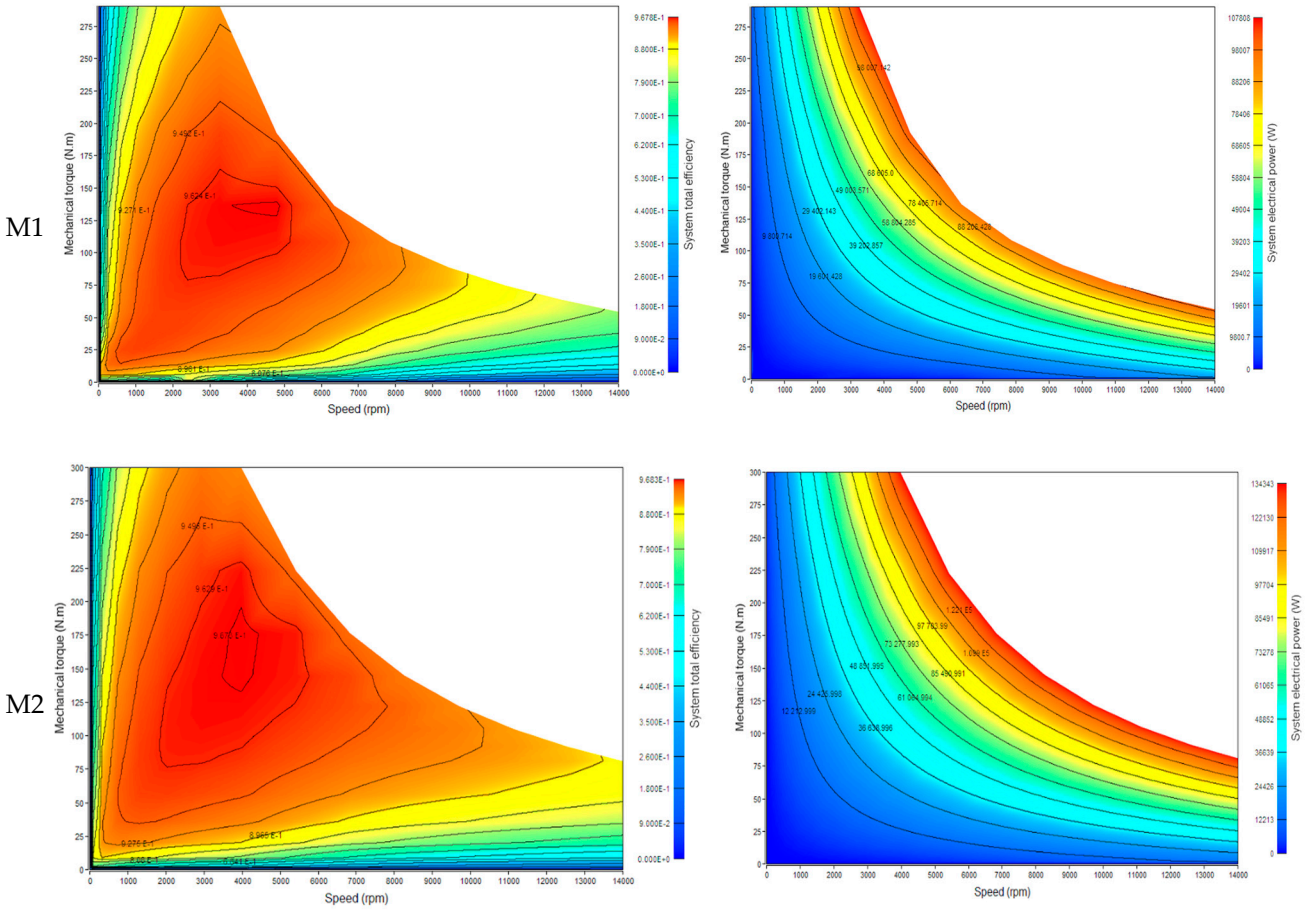


Figure 9. Electromagnetic performance maps of the investigated PMSM traction motors: (**a**) efficiency map; (**b**) absorbed electrical power as a function of torque and speed. Note: Scientific notation is displayed in the software format (e.g., 8E3 corresponds to 8×10^3 and numerical values are displayed in the default software format (without thousand separators)).

A comparative analysis of the efficiency maps highlights distinct functional differences between the two rotor architectures. The M1 configuration exhibits peak efficiency values in

the medium-speed and high-torque region, which corresponds to the dominant operating regimes of the WLTP driving cycle. In these regions, lower current levels are required to deliver the same mechanical power, resulting in reduced Joule losses and improved overall efficiency.

By contrast, the M2 configuration extends the high-efficiency operating region toward higher rotational speeds and demonstrates superior performance under field-weakening conditions. The V-shaped magnet rotor architecture facilitates high-speed operation with more balanced current requirements and a more uniform loss distribution, which is beneficial in terms of thermal stability and extended operation beyond the base speed.

The analysis of total electromagnetic losses further confirms these trends. M1 exhibits higher losses under maximum torque conditions and at elevated speeds, mainly due to the stronger magnetic flux associated with the increased permanent magnet content. In contrast, M2 shows a more gradual increase in losses across the operating range, leading to more favorable thermal behavior during high-speed operation.

The resulting efficiency and loss maps constitute the basis for the subsequent vehicle-level analysis, in which the operating points derived from the vehicle longitudinal dynamic model are superimposed onto the motor performance maps. This procedure enables the evaluation of energy consumption, efficiency distribution, and overall propulsion system performance over the WLTP driving cycle, as well as a comparative assessment of the impact of the two PMSM topologies on the driving range of the electric vehicle.

2.4. Traction Inverter Model and Electrical Losses

Within the energy conversion chain of the electric propulsion system, the traction inverter is responsible for converting the direct current supplied by the battery pack into the three-phase alternating current required by the permanent magnet synchronous motor (PMSM). During regenerative braking operation, the inverter enables bidirectional power flow, allowing the electrical energy generated by the machine to be transferred back to the battery.

In the adopted energy modeling framework, the motor efficiency $\eta_m(\omega_m, T_m)$ accounts exclusively for the internal electromagnetic losses of the PMSM, namely copper losses in the stator windings and magnetic losses in the ferromagnetic core, as derived from the FEM-based efficiency maps. The losses associated with the traction inverter are not included in motor efficiency and are therefore modeled separately, in accordance with common practice in energy-oriented electric vehicle simulations [6,7,21].

The power dissipated in the inverter is modeled as the sum of conduction losses and switching losses, according to the following expression:

$$P_{\text{inv}} = k_{\text{cond}} \cdot I_{\text{line}}^2 + k_{\text{sw}} \cdot f_e \cdot I_{line} \tag{16}$$

where I_{line} denotes the line current corresponding to the operating point, and f_e is the electrical frequency of the rotating magnetic field, defined as: $f_e = p \cdot \frac{n_m(t_k)}{60}$ with p representing the number of pole pairs and n_m the motor rotational speed expressed in revolutions per minute. The coefficients $k_{cond} = 0.02$ W/A^2 and $k_{sw} = 10^{-4}$ W/Hz are employed as lumped parameters to approximate conduction and switching losses, respectively. These coefficients do not correspond to a specific semiconductor technology but rather represent equivalent loss factors commonly adopted in system-level energy simulations, where the focus is placed on overall power flow and relative energy differences rather than on detailed device-level modeling [6,7].

This simplified formulation captures the combined influence of current magnitude and electrical frequency on inverter losses and is particularly suitable for transient operating conditions such as those encountered in standardized driving cycles (e.g., WLTP) [7,9].

In traction mode, the mechanical power required at the wheels P_w is referred to the motor shaft by accounting for the drivetrain efficiency η_{tr}, according to:

$$P_{\text{mec}} = \frac{P_w}{\eta_{\text{tr}}}, \tag{17}$$

where η_{tr} denotes the transmission efficiency.

The electrical power drawn from the battery is then expressed as:

$$P_{\text{bat,out}} = \frac{P_{mec}}{\eta_m(\omega_m, T_m)} + P_{inv} = \frac{P_w}{\eta_{tr} \cdot \eta_m(\omega_m, T_m)} + P_{inv} \tag{18}$$

During regenerative braking, the power flow is reversed, and the inverter operates in bidirectional mode. In this study, the effective regenerative power delivered to the battery is not computed explicitly at inverter level but is determined by the battery and regenerative braking model presented in Section 2.5, which accounts for generator efficiency and system-level limitations. Consequently, inverter losses during regenerative operation are implicitly included through the adopted battery-side formulation.

The inverter model is implemented using efficiency-based loss representation derived from steady-state operating maps, without explicit switching-frequency modeling. The battery is represented using an energy-based model referenced to usable capacity, neglecting detailed electrochemical dynamics. These assumptions are considered appropriate for cycle-level energy analysis but may not capture transient or temperature-dependent effects.

This explicit separation between motor losses, inverter losses, and battery behavior ensures a transparent and consistent formulation of the energy balance and is aligned with established modeling practices for electric vehicle energy consumption analysis [6,7,26].

2.5. Energy Source (Battery) Model and Operational Constraints

The energy source of the analyzed battery electric vehicle is a lithium-ion battery pack based on NMC pouch cells, with a usable energy of 85 kWh. The pack is configured in a 108s5p architecture, meaning that 108 cells are connected in series in each string to reach the required voltage level, while five such strings are connected in parallel to increase the overall capacity and current capability. Assuming a nominal NMC cell voltage of approximately 3.7 V, the 108-series configuration results in a pack voltage compatible with a 400 V traction system. The difference between gross and usable energy reflects the defined state-of-charge operating window implemented to ensure battery durability and lifetime [3,30,32].

The battery is modeled using a simplified equivalent electrical circuit, consisting of an open-circuit voltage source and an internal resistance. The open-circuit voltage of the pack is expressed as a function of SoC as:

$$U_{\text{oc}}(\text{SoC}) = N_s \cdot U_{0,\text{cell}}(\text{SoC}) \tag{19}$$

where N_s denotes the number of series-connected cells and $U_{0,cell}$ is approximated as a piecewise function of SoC based on representative voltage points. Accordingly, the pack open-circuit voltage varies between approximately 362 V at low SoC and 448 V at full charge.

Under load, the battery terminal voltage is given by:

$$U_{\text{bat}} = U_{\text{oc}}(\text{SoC}) - R_{\text{int}} \cdot I_{\text{bat}} \tag{20}$$

with R_{int} represents the equivalent internal resistance of the battery pack.

For the WLTP-based simulations, the initial state of charge is set to SoC = 100%. Owing to the limited SoC variation over a single WLTP cycle, the open-circuit voltage is assumed quasi-constant during one cycle, and its average value is used for computing battery current, voltage drop, and power balance. This assumption is consistent with common practice in cycle-level energy simulations and does not affect the comparative nature of the analysis between the two PMSM configurations. This modeling approach is widely adopted in energy-oriented electric vehicle simulations due to its robustness and low computational burden [5,9,32].

The instantaneous electrical power at the battery terminals is defined as:

$$P_{\text{bat}} = U_{\text{bat}} \cdot I_{\text{bat}} \tag{21}$$

The battery current is obtained by solving the corresponding power balance equation:

$$R_{\text{int}} \cdot I_{\text{bat}}^2 - U_{\text{oc}} \cdot I_{\text{bat}} + P_{\text{bat}} = 0 \tag{22}$$

which yields:

$$I_{\text{bat}} = \frac{U_{\text{oc}} - \sqrt{U_{\text{oc}}^2 - 4 \cdot R_{\text{int}} \cdot P_{\text{bat}}}}{2 \cdot R_{\text{int}}} \tag{23}$$

This formulation enables the direct computation of battery currents in both traction (discharge) and regenerative braking (charge) modes and provides a consistent basis for evaluating battery losses and power limitations.

Regenerative braking is modeled explicitly through the reversal of power flow whenever the longitudinal acceleration becomes negative and the mechanical power at the wheels is negative. Under these conditions, the power flow follows the sequence: wheels → transmission → motor → inverter → battery.

The electromechanical energy conversion efficiency during regenerative braking is evaluated pointwise using the FEM-derived motor efficiency maps. Instead of computing a dedicated generator-mode FEM map, the generator efficiency is approximated by mirroring the motoring efficiency map and applying a correction factor $k_{regen} = 0.95$, such as:

$$\eta_{\text{m,gen}}(\omega_m, T_m) = k_{\text{regen}} \cdot \eta_{\text{m}}(\omega_m, T_m) \tag{24}$$

This correction accounts for the additional losses associated with generator operation and control, while preserving the spatial distribution of efficiency obtained from the electromagnetic analysis.

At system level, a global regenerative efficiency factor $\eta_{sys,regen} = 0.70$ is introduced to account for the fact that only a fraction of the mechanically available braking energy is effectively recovered and transferred to the battery. This factor represents the combined effects of brake blending with mechanical brakes, battery charging power limitations, and SoC and thermal constraints imposed by the BMS, and is independent of the PMSM electromagnetic efficiency.

The electrical power injected into the battery during regenerative braking is expressed as:

$$P_{\text{bat,regen}} = -P_{\text{mec}} \cdot \eta_{m,\text{gen}} \cdot \eta_{\text{sys,regen}} \tag{25}$$

where $\eta_{m,gen}$ is evaluated at the instantaneous operating point (ω_m, T_m).

The corresponding regenerative battery current is obtained as:

$$I_{bat,regen} = -\frac{P_{\text{bat},regen}}{U_{\text{bat}}} \tag{26}$$

For the investigated configuration, it is assumed that battery current, SoC, and temperature limits imposed by the BMS are not reached over the WLTP cycle, such that regenerative braking is governed primarily by the dynamic requirements of the driving profile. This assumption is consistent with previous studies on cycle-level energy consumption of compact-class BEVs [5,9,27].

This battery and regenerative braking modeling approach provides a consistent and sufficiently accurate representation of energy extraction and recuperation, while avoiding unnecessary complexity relative to the main objective of the study, namely the comparative assessment of the energy performance of the two PMSM rotor topologies. The resulting battery power and current profiles constitute the basis for the WLTP-based energy balance and driving range evaluation presented in the following section.

2.6. WLTP Driving Cycle and Integrated Energy Simulation Procedure

The energy performance of the analyzed battery electric vehicle is evaluated by simulating its operation over the Worldwide Harmonized Light Vehicles Test Procedure (WLTP), which is adopted as an international reference for the assessment of energy consumption and driving range of electric vehicles [24,33].

The WLTP driving cycle is defined by a longitudinal vehicle speed profile $v(t)$ applied over a total duration of $T = 1800$ s, corresponding to a traveled distance of $d_{\text{cycle}} = 23.3$ km. The cycle includes representative urban, extra-urban, and high-speed driving phases, covering a wide range of operating conditions relevant for compact-class BEVs [24,25,34].

The energy simulation is performed using a deterministic, sequential workflow in which the imposed speed profile is successively transformed into mechanical and electrical quantities along the propulsion chain. Starting from the WLTP speed profile, the longitudinal vehicle model provides the required traction or braking forces at the wheels. These are then converted into mechanical torque and speed demands at the electric motor shaft, which are mapped onto the FEM-derived motor efficiency and current maps. Subsequently, inverter losses and battery electrical behavior are considered to determine the instantaneous battery power and current.

The overall structure of the energy simulation procedure, including the interaction between the WLTP driving cycle, the longitudinal vehicle dynamics, the electric motor, the traction inverter, and the battery model, is summarized in Figure 10.

The battery power P_{bat} constitutes the central quantity for the cycle-level energy balance. Positive battery power corresponds to traction operation and battery discharge, while negative battery power corresponds to regenerative braking and battery charging. The battery current is used consistently throughout the WLTP simulation.

The electrical energy exchanged with the battery over one driving cycle is obtained by integrating the battery power over time. In the numerical implementation, this integral is evaluated using a discrete summation over the WLTP time steps. The energy consumed from the battery is computed as:

$$E_{\text{cons}} = \int_0^T P_{bat,out,}(t) \cdot dt \approx \sum_{k=1}^{N} P_{\text{bat,out}}(t_k) \cdot \Delta t \tag{27}$$

Similarly, the total energy recovered through regenerative braking is computed by integrating the negative battery power:

$$E_{\text{regen}} = \int_o^T P_{bat,regen}(t) \cdot dt \approx \sum_{k=1}^{N} P_{\text{bat,regen}}(t_k) \cdot \Delta t \tag{28}$$

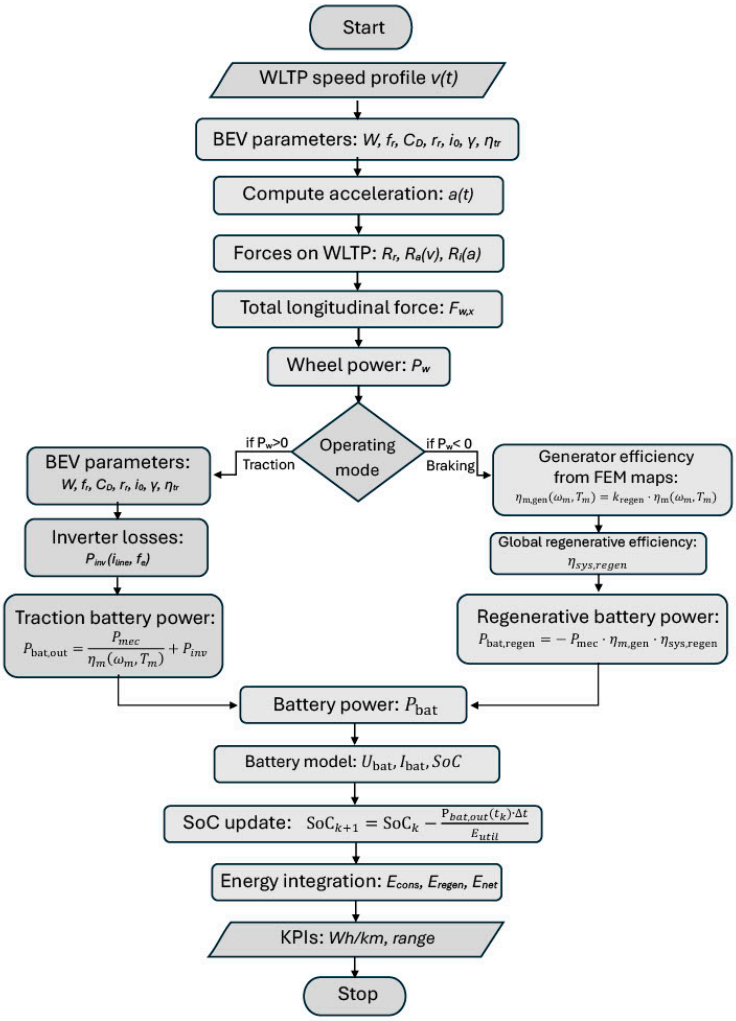


Figure 10. Flowchart of the proposed WLTP-based vehicle energy evaluation framework.

The net electrical energy extracted from the battery over one WLTP cycle is then expressed as:

$$E_{\text{net}} = E_{\text{cons}} - E_{\text{regen}} \tag{29}$$

The evolution of the battery state of charge is determined from the incremental energy balance, referenced to the usable battery energy E_{util}:

$$\text{SoC}_{k+1} = \text{SoC}_k - \frac{\text{P}_{bat,out}(t_k)\cdot\Delta t}{E_{util}} \tag{30}$$

This formulation naturally accounts for both discharge and recharge phases and ensures energetic consistency over the entire driving cycle [5,9].

Based on net energy consumption and the WLTP cycle distance, the specific energy consumption is calculated as:

$$C_{\text{WLTP}} = \frac{E_{\text{net}}}{d_{\text{cycle}}}[\text{Wh/km}] \tag{31}$$

The driving range is subsequently estimated as:

$$A \approx \frac{E_{\text{util}}}{E_{net}/d_{\text{cycle}}}[\text{km}] \tag{32}$$

The approximation in (27) and (28) results from the discrete-time integration of battery power using the WLTP sampling interval (Δt = 1 s). Given the relatively smooth variation in battery power over the driving cycle and the high temporal resolution of the WLTP speed profile, the numerical integration error is negligible compared to other modeling uncertainties, such as drivetrain efficiency assumptions and aerodynamic parameters.

Equation (32) assumes that the specific energy consumption obtained over one WLTP cycle is representative and scales linearly with the usable battery energy. This approximation neglects certain second-order effects, such as state-of-charge-dependent efficiency variations or thermal drift during extended operation. However, since the analysis is performed under identical boundary conditions for both motor topologies, this approximation does not affect the relative comparison, which constitutes the primary objective of this study.

The proposed WLTP-based simulation framework enables a coherent and reproducible evaluation of energy consumption, recuperated energy, and driving range, while maintaining a clear separation between component-level models and cycle-level energy accounting. By directly linking the FEM-derived electromagnetic performance of the PMSM traction motors to realistic vehicle operating conditions, the methodology provides a robust basis for the comparative energy assessment of the investigated motor topologies, in line with state-of-the-art BEV energy simulation approaches [4–6,9–12].

The above formulation provides a consistent description of the vehicle longitudinal dynamics, drivetrain power flow, and battery energy balance used in the WLTP-based simulations. This integrated approach enables the evaluation of rotor topology effects on vehicle-level energy consumption and driving range under realistic operating conditions.

3. Results

3.1. Comparative Analysis of PMSM Operating Points and Efficiency over the WLTP Cycle

The comparative analysis of the energy consumption of an electric vehicle equipped with the two previously analyzed permanent magnet synchronous motor (PMSM) variants was performed by projecting the operating points derived from the WLTP driving cycle onto the efficiency maps obtained from FEM-based electromagnetic simulations. This approach enables a direct assessment of the distribution of motor operating regimes and the associated efficiency levels under representative driving conditions.

The efficiency maps of M1 and M2 were integrated into a dynamic Matlab2023a/Simulink model, in which the motor operating points, defined by the pairs (n_m, T_m), were computed based on the WLTP speed profile. For regenerative braking operation, the efficiency maps were symmetrically extended into the negative torque domain, with a correction applied to account for inverter-related losses.

Figure 11 shows the superposition of the traction motor operating points on the efficiency maps for the two PMSM topologies analyzed. For both variants, the operating points are predominantly concentrated in the low- and medium-speed regions, below approximately 5000 rpm, and at moderate torque levels. These regions correspond mainly to the urban and extra-urban phases of the WLTP cycle. In these operating domains, both motors operate at high efficiency, typically exceeding 85% and frequently surpassing 90%.

Operating points associated with very high speeds or peak torque values appear only sporadically and represent a limited fraction of the total cycle duration. These regimes are mainly associated with short acceleration events or rapid transitions between WLTP phases and do not constitute dominant operating conditions. This distribution indicates that the WLTP energy demand is concentrated in efficiency-favorable operating regions of the traction motors.

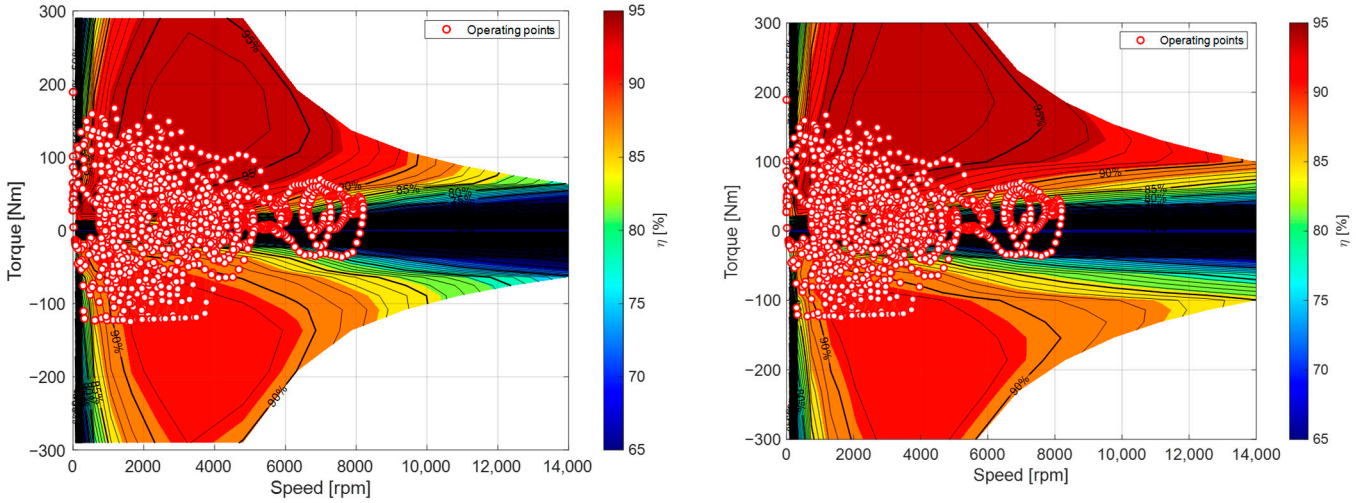


Figure 11. Superposition of traction motor operating points derived from the WLTP speed profile on to the motor efficiency maps.

The statistical distribution of operating points and the corresponding average efficiencies for both PMSM configurations are summarized in Table 4. In low-load regimes (0–50 Nm), representative of urban driving, both motors exhibit high efficiency at low speeds. However, M1 maintains higher average efficiency values than M2 in the medium-speed range (1000–5000 rpm) and at higher speeds (5000–8000 rpm). The statistical distribution of the operating points and the corresponding average efficiencies for both PMSM configurations over the WLTP cycle are summarized in Table 5.

Table 5. Summary of operating point distribution and average efficiency of M1 and M2 over the WLTP driving cycle.

Operating Regime	Speed Range [rpm]	Torque Range [Nm]	M1 $\eta_{average}$ [%]	M2 $\eta_{average}$ [%]	Main Observation
Low load (urban)	0–1000	0–50	~85.4	~84.1	Comparable efficiency at very low speed and torque
Low load (urban/cruise)	1000–5000	0–50	~81.7	~72.6	M1 maintains significantly higher efficiency
Low load (high speed)	5000–8000	0–50	~75.5	~68.9	Both outside optimal zone; M1 less penalized
Medium load (extra-urban)	1000–5000	50–100	~95.6	~94.9	Both operate in optimal efficiency region
High load (acceleration)	1000–5000	100–150	~95.8	~96.1	Similar peak efficiencies, rare operating points
Regenerative braking	1000–5000	−50 to −150	87–91	87–91	Efficient regeneration for both topologies
Regeneration at high speed	5000–8000	−50 to −150	~69.0	~63.0	Efficiency drop, more pronounced for M2

In low-load regimes (0–50 Nm), representative of urban driving, both motors exhibit high efficiency at low speeds. However, M1 maintains higher average efficiency values than M2 in the medium-speed range (1000–5000 rpm) and at higher speeds (5000–8000 rpm).

For medium-load conditions (50–100 Nm), associated primarily with extra-urban driving, both motors operate within their optimal efficiency region, achieving average efficiencies above 94% in the 1000–5000 rpm range. These operating conditions represent

the dominant contribution to the WLTP cycle. At higher load levels (above 100 Nm), both configurations maintain high efficiency at medium speeds, although these operating points occur infrequently and have a limited influence on total energy consumption.

In regenerative braking operation, corresponding to negative torque values, both PMSM configurations exhibit average electromagnetic efficiencies between approximately 87% and 91% in the 1000–5000 rpm range. At higher speeds, regenerative efficiency decreases for both motors, with a more pronounced reduction observed for M2. These operating regimes, however, account for a small portion of the WLTP cycle.

The temporal evolution of instantaneous motor efficiency over the WLTP cycle is presented in Figure 12. Rapid efficiency variations are observed due to frequent transitions of the operating point in the speed–torque plane. Both motors frequently reach instantaneous efficiency values above 90% and, in some intervals, above 95%. M1 exhibits a narrower dispersion of efficiency values and sustains high efficiency over longer time intervals.

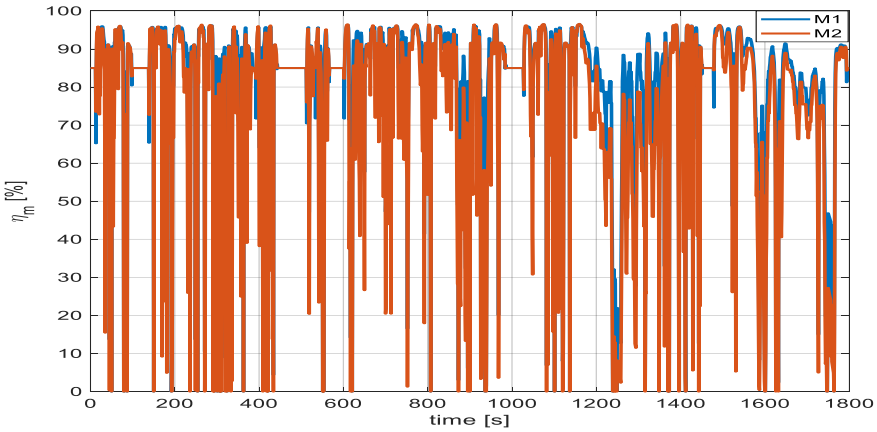


Figure 12. Temporal evolution of instantaneous motor efficiency over the WLTP cycle.

The weighted average efficiency over the entire WLTP cycle, reported in Table 6, is approximately 88.85% for M1 and 84.56% for M2. This difference reflects the distinct distribution of operating points across the efficiency maps for the two configurations.

Table 6. Average efficiency of motors over the entire WLTP cycle.

Motor Variant	$\eta_{average}$ [%]	Observation
M1	~88.85%	Higher overall efficiency; stable efficiency across typical WLTP operating conditions.
M2	~84.56%	Slightly lower overall efficiency; reduced efficiency during acceleration and braking events.

The correlation between the efficiency maps and the temporal evolution of efficiency indicates that local reductions in instantaneous efficiency are directly associated with transient transitions of the operating trajectory into less favorable energetic regions. Conversely, intervals characterized by high and stable efficiency correspond to periods during which the operating points remain concentrated within the maximum-efficiency regions of the FEM-derived maps.

3.2. Battery Power, Current, and Energy Balance over the WLTP Cycle

The distribution of electrical power drawn from the battery and injected into the battery through regenerative braking during vehicle operation over the WLTP driving cycle is shown in Figure 13. The battery power profile exhibits a mixed WLTP pattern,

characterized by extended intervals at low to moderate power levels and short-duration peaks at higher power demand.

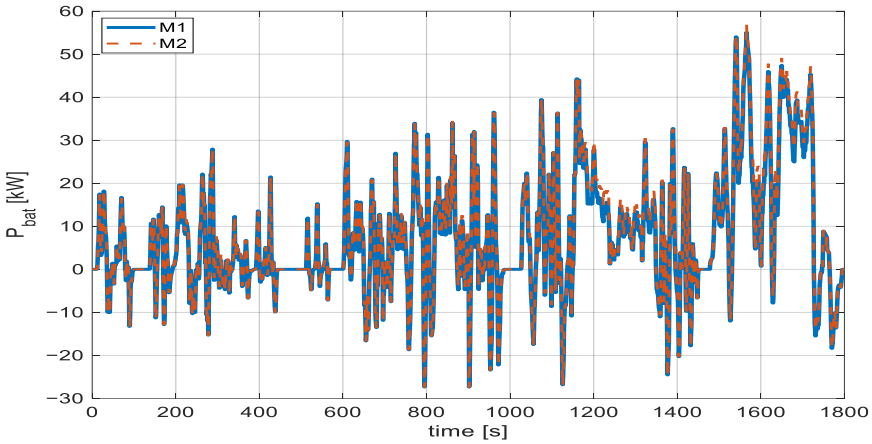


Figure 13. Battery power profile over the WLTP driving cycle (traction and regenerative braking).

During traction operation, the battery power demand remains predominantly below 20 kW. Power peaks occur mainly during acceleration phases and high-speed segments, reaching maximum values of approximately 55–57 kW. These events are limited in duration and represent a small fraction of the total cycle time.

During regenerative braking, the electrical power injected into the battery is concentrated mainly in the range of 5–20 kW (absolute values). Higher regenerative power pulses, reaching up to approximately 30 kW, occur only occasionally and are associated with more intense deceleration events in the urban and extra-urban phases of the WLTP cycle.

For the analyzed simulation conditions (WLTP cycle, transmission ratio $i_{tr} = 8$, current limit $I_{max} = 250$ A), the battery power delivered closely matches the power demand of the propulsion system. No discrepancies between requested and delivered power are observed, and no current limitation events occur. The maximum battery discharge current reaches approximately 131 A, while the minimum battery terminal voltage remains around 441 V, assuming an internal resistance of $R_{int} = 0.02\ \Omega$.

The differences between the two motor variants are reflected in the magnitude of the electrical power requested from the battery. The average absolute difference in requested battery power is approximately 0.735 kW, with a 95th-percentile value of 3.223 kW and a maximum difference of 6.195 kW. These deviations occur primarily during high-load operating windows.

The spatial distribution of electrical energy processed by the battery is shown in Figure 14. Traction energy is mainly accumulated at higher rotational speeds and moderate torque levels, while regenerated energy is concentrated at low to medium speeds combined with high negative torque values. The distribution of operating points in the (n_m, T_m) plane is similar for both motor variants.

Figure 15 shows the time evolution of the battery terminal current over the WLTP cycle. Peak discharge currents reach approximately 127–130 A, whereas regenerative currents typically remain within -50 to -65 A. The current profiles of the two motor variants are nearly identical over the entire cycle.

As shown in Figure 16 compares the battery terminal current with the stator winding line current of the electric motor. The motor line current reaches higher peak values, typically between 100 and 200 A, reflecting the DC/AC conversion performed by the inverter. In all cases, the battery current remains well below the imposed current limit.

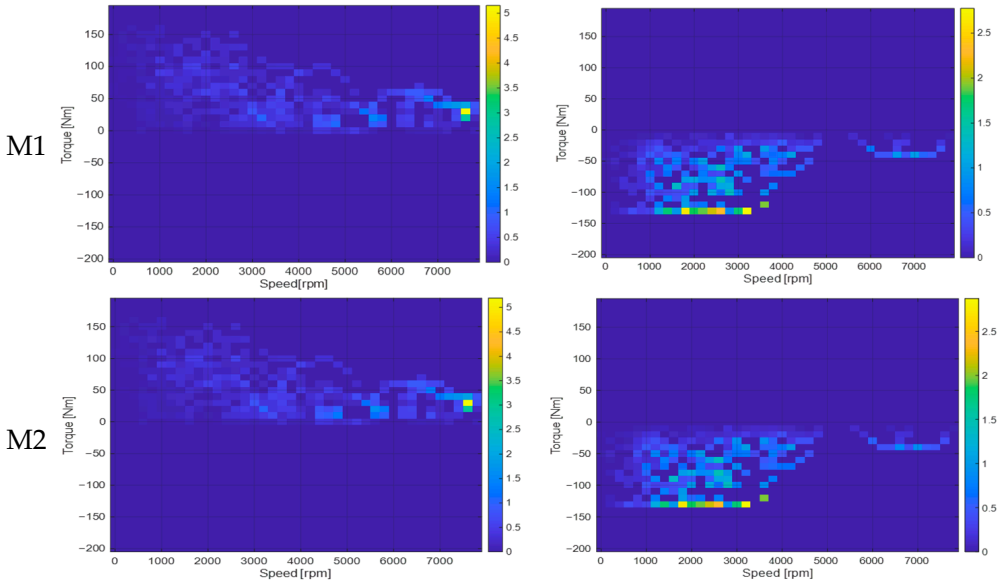


Figure 14. Spatial distribution of electrical energy processed by the battery in the motor speed–torque domain over the WLTP cycle: (**a**) traction energy; (**b**) regenerated energy.

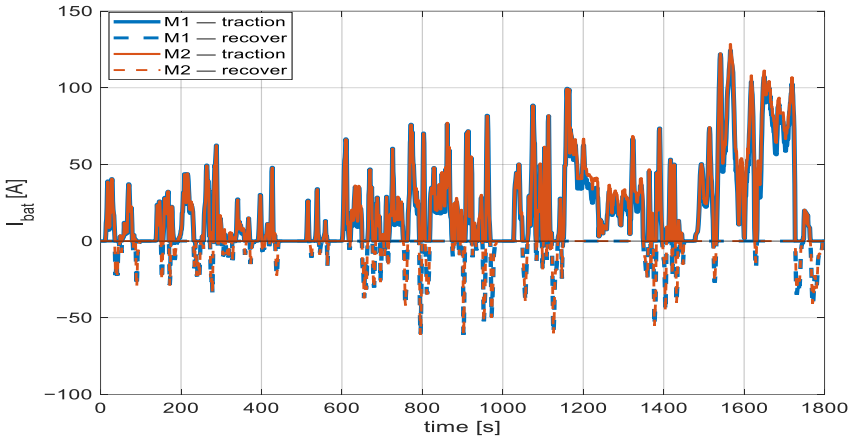


Figure 15. Time evolution of the battery terminal current over the WLTP driving cycle.

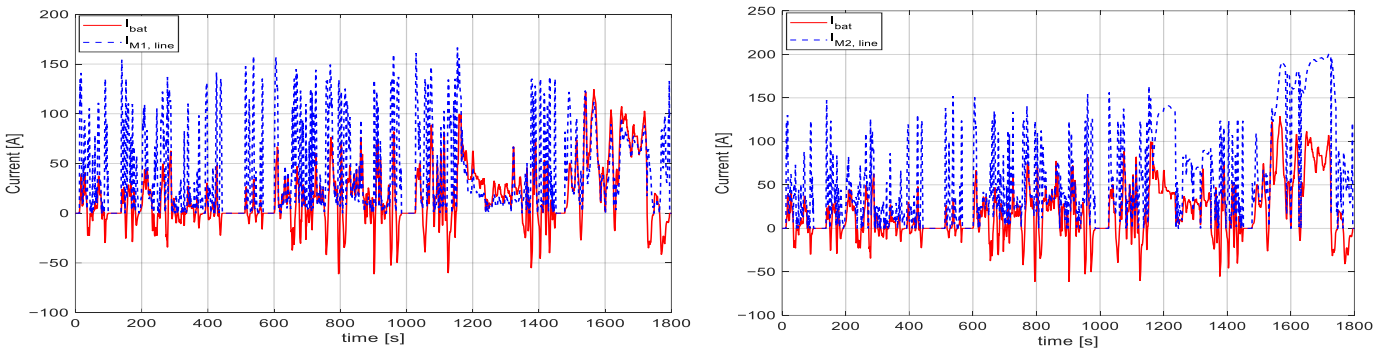
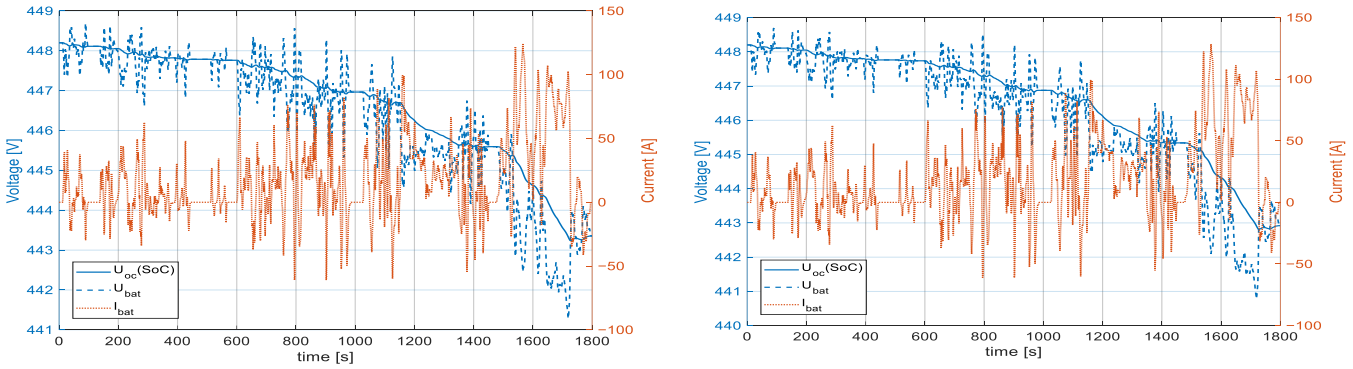


Figure 16. Comparison between the battery terminal current and the motor stator line current over the WLTP driving cycle.

Figure 17 shows the battery open-circuit voltage, terminal voltage, and current profiles. For M1, the average, 95th-percentile, and maximum voltage sag are 0.41 V, 1.64 V, and 2.53 V, respectively, while for M2 they are 0.71 V, 1.71 V, and 2.62 V. The RMS battery current

equals 35.1 A for M1 and 36.93 A for M2, leading to ohmic losses of 12.3 Wh and 13.6 Wh, respectively.

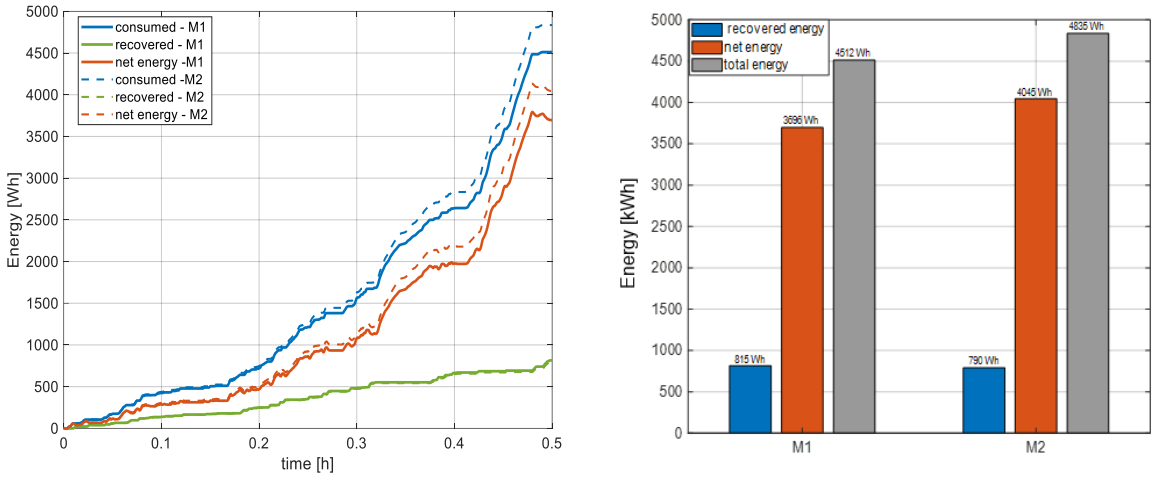


(M1) (M2)

Figure 17. Evolution of battery open-circuit voltage, terminal voltage, and current over the WLTP driving cycle.

3.3. Regenerative Braking Contribution

Figure 18a illustrates the cumulative evolution of traction energy consumption and energy recovered through regenerative braking over the WLTP cycle. The traction energy increases almost linearly with driving time, while regenerative braking introduces local reductions in the net energy extracted from the battery during deceleration phases.



(**a**) (**b**)

Figure 18. Comparison of cumulative traction energy consumption, recovered energy, and net energy for M1 and M2 over the WLTP driving cycle: (**a**) cumulative energy evolution over time; (**b**) total energy balance per WLTP cycle (right) for M1 and PMS.

Figure 18b summarizes the integrated energy values. For M1, the traction energy is 4512 Wh, the recovered energy is 815 Wh, and the net energy extracted from the battery is 3696 Wh. For M2, the corresponding values are 4835 Wh, 790 Wh, and 4045 Wh. The difference in recovered energy between the two variants is limited, amounting to approximately 25 Wh (≈3%), whereas the difference in net energy is 349 Wh, corresponding to a reduction of approximately 9.14% in favor of M1. The ratio between recovered energy and traction energy is approximately 18% for M1 and 16% for M2.

Figure 19 presents the evolution of the battery state of charge (SoC) over the WLTP cycle. When regenerative braking is enabled, the final SoC increases by approximately

0.9–1.0 percentage points (pp) for both motor variants. The difference in final SoC between M1 and M2 under regenerative braking conditions is approximately 0.35–0.45 pp.

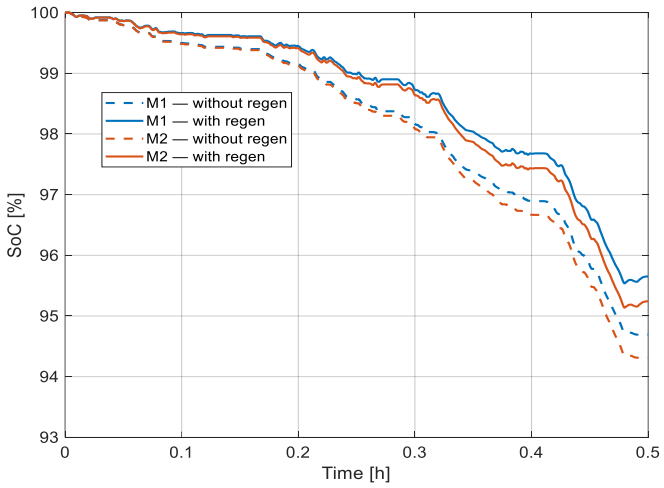
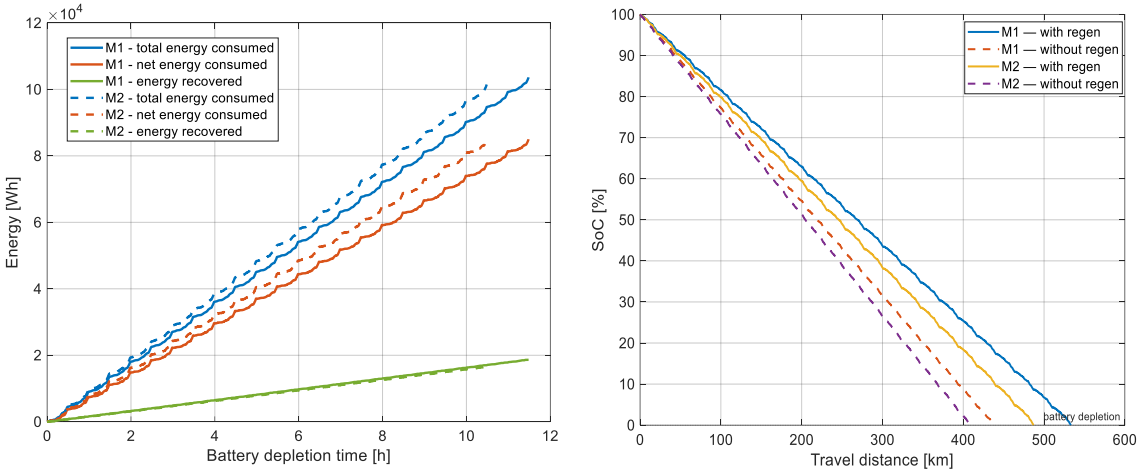


Figure 19. Evolution of the battery state of charge (SOC) over the WLTP cycle.

These results indicate that, under the WLTP driving cycle and the imposed battery constraints, the two motor variants exhibit similar regenerative energy recovery levels, while the differences in net energy consumption and final SoC are primarily driven by the traction energy demand.

3.4. WLTP Energy Consumption and Driving Range

The driving range of the BEV can be estimated from the net battery energy consumption over the WLTP cycle and the usable battery capacity. Figure 20 depicts the cumulative energy evolution over repeated WLTP cycles with and without regenerative braking. In both motor variants, cumulative energy increases nearly linearly with the number of cycles, while regenerative braking reduces the slope of this trend due to recovered energy during deceleration. For identical driving conditions, M2 consistently exhibits higher cumulative energy demand than M1.



(**a**) (**b**)

Figure 20. Impact of regenerative braking on energy depletion and driving range for M1 and M2: (**a**) Energy consumption until battery depletion (**b**) state-of-charge evolution versus driving distance (**b**) for M1 and M2 with and without regenerative.

Figure 21 presents the specific energy consumption and the estimated driving range. M1 exhibits lower specific energy consumption than M2, both with regenerative braking (approximately 159 Wh/km versus 174 Wh/km) and without regenerative braking (approximately 194 Wh/km versus 208 Wh/km). With regenerative braking, the estimated driving range is approximately 535 km for M1 and 489 km for M2. Without regenerative braking, the corresponding values are approximately 438 km and 409 km, respectively.

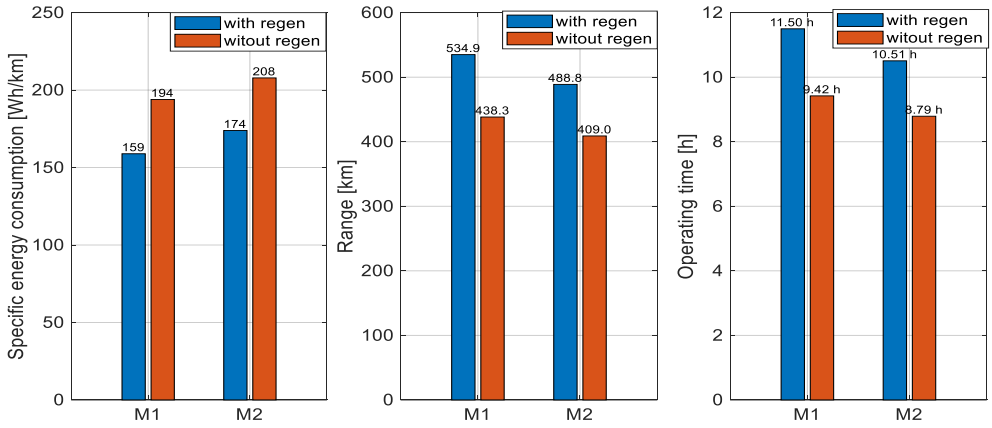


Figure 21. Comparison of BEV key performance indicators (KPIs) for M1 and M2 with and without regenerative braking.

3.5. Comparative Performance Synthesis of the Investigated PMSM Configurations

This subsection provides a concise synthesis of the WLTP-based results obtained for the two PMSM traction motor configurations under identical vehicle parameters, battery characteristics, inverter constraints, and control strategies.

Both propulsion systems operate within similar speed–torque domains imposed by the WLTP driving cycle and the fixed transmission ratio. Quantitative differences are observed in net electrical energy consumption, efficiency distribution, and battery utilization. The M1 configuration consistently exhibits lower net energy consumption per cycle, reduced specific energy consumption, and a higher achievable driving range compared to M2.

Battery power and current profiles confirm that both configurations operate within electrical limits, without current saturation or voltage constraints. M1 shows slightly lower RMS battery currents, reduced voltage sag, and lower integrated ohmic losses. Regenerative braking performance is comparable for both configurations, with similar amounts of recovered energy and recovery ratios.

The driving range is significantly increased by regenerative braking for both motor configurations (Figure 21). For M1, the range rises from 438.3 km (without regeneration) to 534.9 km (with regeneration), corresponding to an improvement of approximately 22%. For M2, the range increases from 409.0 km to 488.8 km, i.e., by about 19.5%.

The adopted vehicle parameters and the resulting specific energy consumption values fall within the typical range reported for compact-class BEVs under WLTP conditions (150–200 Wh/km), confirming the physical consistency of the simulation framework.

In both operating scenarios, M1 achieves a higher driving range than M2, confirming the superior energy efficiency of the dual-layer IPM rotor configuration.

4. Discussion

4.1. Impact of Rotor Topology on Operating Point Distribution and WLTP Efficiency

The obtained results highlight the influence of rotor architecture on the distribution of PMSM operating points over the WLTP driving cycle and on the overall energy efficiency of the electric vehicle. The two investigated motor configurations are comparable in terms

of dimensions, total mass, and rated power. However, differences in magnetic topology lead to distinct behaviors under real operating conditions.

A first key aspect concerns the correlation between the WLTP-imposed operating point distribution and the regions of maximum efficiency identified on the FEM-derived efficiency maps. The analysis indicates that vehicle operation is dominated by low- and medium-speed regimes combined with moderate torque levels, which are characteristic of urban and extra-urban driving. In this operating domain, M1 exhibits a structural advantage by maintaining higher and more stable efficiency levels even outside the strictly optimal efficiency region, particularly at medium speeds and low loads that frequently occur in everyday vehicle use.

The approximately 4% difference in average efficiency between M1 and M2 over the WLTP cycle becomes relevant at the system level as it accumulates over long operating durations and across many operating points.

In contrast, M2 exploits its structural advantages mainly in the medium- to high-load domain and at higher rotational speeds, where the V-shaped rotor architecture enables more efficient operation under field-weakening conditions. However, these operating regimes are only weakly represented in the WLTP cycle, which explains why the local efficiency advantages of M2 do not translate into a global energy benefit over the analyzed driving cycle.

The behavior under regenerative braking further confirms the differences between the two rotor topologies. Both motors exhibit high regenerative electromagnetic efficiency in the medium-speed range, which dominates the WLTP cycle. Nevertheless, at higher speeds, M1 maintains more favorable regenerative efficiency values.

The temporal evolution of instantaneous efficiency highlights the superior stability of M1, characterized by reduced fluctuations and frequent maintenance of efficiency levels above 90%. From an operational standpoint, this stability is an important indicator of thermal loading and robustness, as large efficiency variations are associated with corresponding variations in losses and thermal fluxes within the motor and inverter.

From a techno-economic perspective, the results confirm the existence of a clear trade-off between permanent magnet mass reduction and energy efficiency. M2 reduces the amount of NdFeB material and dependency on critical raw materials; however, this benefit is partially offset by a slightly lower global efficiency over the WLTP cycle. In contrast, M1 employs a larger amount of permanent magnet material but delivers more favorable energy behavior, particularly in urban and peri-urban driving.

It should be noted that the obtained results depend on the selected transmission ratio and the adopted control strategy. In this study, a standard MTPV strategy and a fixed transmission ratio representative of compact BEVs were employed. Further optimization of these parameters could alter the operating point distribution and potentially reduce the observed differences between the two motor topologies. Moreover, the analysis is limited to the WLTP cycle and does not include aggressive driving scenarios or sustained high-speed operation, where the advantages of M2 may become more pronounced.

4.2. Battery Load and System-Level Implications

The comparative analysis of battery power, current, and energy balance over the WLTP driving cycle provides valuable insight into how PMSM rotor topology influences battery loading and the overall efficiency of the propulsion system. Since vehicle dynamics, transmission ratio, inverter constraints, control strategy, and battery parameters are identical for both configurations, the observed differences can be directly attributed to the electromagnetic and efficiency characteristics of the two motor designs.

The WLTP power demand profile is dominated by extended intervals at low to moderate battery power levels, interspersed with short-duration peaks associated with acceleration events and high-speed operation. Peak traction power at the battery terminals reaches approximately 55–57 kW, while regenerative braking power is mainly concentrated in the 5–20 kW range. This distribution confirms that the WLTP cycle imposes moderate average electrical loading on the battery, with limited exposure to extreme operating conditions. Consequently, both propulsion system configurations operate well within the electrical and thermal limits of the battery pack and inverter, indicating that the system is appropriately dimensioned for the targeted BEV application.

A key outcome of the analysis is that no current or voltage limiting occurs throughout the WLTP cycle. The maximum battery current remains well below the imposed limit of 250 A, with peak discharge currents of approximately 127–131 A and regenerative currents in the range of -50 to -60 A. The absence of current saturation or voltage curtailment indicates that the battery does not act as a performance constraint under the conditions investigated. As a result, the differences observed between M1 and M2 arise exclusively from differences in the electrical power required to meet identical mechanical demands at the wheels, rather than from battery-side limitations.

At the system level, M2 exhibits a slightly higher average battery power demand than M1, particularly during high-load operating intervals. The mean absolute difference in required battery power is approximately 0.7 kW, with a 95th percentile below 3 kW and occasional peaks approaching 6.34 kW. Although these deviations correspond to up to 10% of the instantaneous peak power, they occur infrequently and remain modest relative to the overall power level. Nevertheless, when integrated over the entire WLTP cycle, these differences result in a measurable increase in total energy drawn from the battery for M2.

M1 maintains slightly higher efficiency and lower current demand in operating regions associated with elevated torque and speed, which coincides with peak battery power demand. In contrast, M2, while advantageous in terms of permanent magnet mass reduction and high-speed field-weakening capability, exhibits marginally higher electrical losses in these regions, leading to increased battery power demand and higher RMS current.

The temporal evolution of the battery current for both motor variants shows nearly overlapping profiles over most of the WLTP cycle, with small but systematic deviations during high-load segments, where M2 tends to draw slightly higher current. These differences are reflected in higher RMS current values for M2, which in turn lead to increased integrated ohmic losses within the battery, despite identical internal resistance and operating conditions.

Voltage sag statistics reinforce this conclusion. Although the absolute voltage drop at the battery terminals remains moderate for both configurations, M2 exhibits slightly higher average and peak voltage sag, as well as a greater proportion of operating time at elevated sag levels. While these differences are not critical under WLTP conditions, they indicate a less uniform electrical loading of the battery and increased internal dissipation. Over extended operation, such effects may contribute to higher thermal stress and accelerated battery aging.

The spatial distribution of energy flow in the speed–torque plane confirms that these effects are not driven by differences in vehicle operation. The operating point distribution is nearly identical for both variants and is dictated by the WLTP cycle and the fixed transmission ratio. However, M2 shows slightly higher energy weight in high-speed regions, consistent with its increased battery power demand in those conditions.

4.3. Contribution and Limits of Regenerative Braking

The contribution of regenerative braking to the overall energy balance of the battery electric vehicle was evaluated by comparing the total traction energy, the recovered energy, and the net energy extracted from the battery over the WLTP driving cycle. The cumulative evolution of these quantities highlights the nearly linear growth of traction energy typical of standardized driving cycles, as well as the role of regenerative braking in locally reducing the net energy demand by recovering a fraction of the vehicle's kinetic energy during deceleration phases.

For the same WLTP profile and identical battery constraints (nominal voltage, internal resistance, and current limits), the two PMSM configurations exhibit very similar amounts of recovered energy: approximately 815 Wh for M1 and 790 Wh for M2. The relatively small difference (≈3%) indicates that the regenerative braking capability is only weakly influenced by the rotor topology under WLTP conditions.

In contrast, significant differences emerge in traction energy consumption. The total energy required for propulsion prior to subtracting the regenerative contribution amounts to approximately 4512 Wh for M1 and 4835 Wh for M2, leading to a net energy difference of about 349 Wh (≈9.14%) in favor of M1.

The fraction of recovered energy relative to traction energy further supports this conclusion. The ratio $E_{\mathrm{reg}}/E_{\mathrm{cons}}$ is approximately 18% for M1 and 16% for M2. Both values fall within the typical range reported for WLTP-based BEV assessments (≈15–25%), corresponding to an overall regenerative efficiency on the order of 65–80%.

When referenced to the global regenerative efficiency adopted in the model (η_{regen} = 0.70), the recovered electrical energies correspond to available mechanical braking energies of approximately 1.16 kWh for M1 and 1.10 kWh for M2 per WLTP cycle. A hypothetical increase in regenerative efficiency from 0.70 to 0.80 would yield an additional recovered energy of 0.12 kWh for M1 and 0.11 kWh for M2 per cycle, translating into a net energy reduction of only about 5%.

The evolution of the battery state of charge over the WLTP cycle confirms that regenerative braking increases the final SoC by approximately 0.9–1.0 percentage points for both configurations, directly consistent with the recovered energy values. The remaining SoC difference between M1 and M2 under regenerative conditions (≈ 0.35–0.45 pp) corresponds to an energy surplus of about 350 Wh and is primarily attributable to reduced traction losses in M1.

4.4. Implications for Driving Range and Powertrain Design

The WLTP-based energy analysis indicates that, although both motor configurations recover comparable amounts of energy during deceleration, the M1 configuration consistently achieves lower net energy consumption per cycle, resulting in an extended driving range. This advantage originates from the distribution of operating points imposed by the WLTP cycle and their alignment with the respective efficiency maps. For identical wheel-level mechanical demands, M1 operates more frequently in high-efficiency regions and requires lower current, which reduces Joule losses in the motor, inverter, and battery and leads to more stable voltage behavior. Conversely, M2 exhibits higher current demand in certain operating regions, particularly at elevated speeds, thereby increasing ohmic losses and overall battery energy extraction.

When integrated over a complete driving cycle and extrapolated to full battery depletion, these effects accumulate and yield measurable differences in total energy consumption and driving range. The nearly constant ratio between recovered and consumed energy supports the representativeness of single-cycle WLTP results for extended operation, indicating that the observed differences are structural rather than cycle-specific.

From a powertrain design perspective, the results demonstrate that reducing permanent magnet mass does not necessarily lead to lower energy consumption. While the M2 configuration offers advantages in terms of rare-earth material reduction and high-speed capability, these benefits are only marginally exploited under WLTP conditions, where low-to-medium speed and moderate torque operation dominates. In contrast, the M1 configuration is better matched to these prevailing operating regimes.

The results further show that regenerative braking plays a major role in extending the driving range of the BEV investigated, regardless of PMSM rotor topology. For the M1 configuration, the activation of regenerative braking increases the range from 438.3 km to 534.9 km, corresponding to a relative improvement of approximately 22%. A similar trend is observed for the M2 configuration, for which the range increases from 409.0 km to 488.8 km, i.e., by about 19.5%.

Beyond the effect of regeneration, a systematic difference between the two motor topologies is observed. In both cases (with and without regenerative braking), the M1 motor provides a higher driving range than M2. This behavior can be attributed to the higher average electromagnetic efficiency of the dual-layer IPM rotor, particularly in the low- and medium-speed operating regions that dominate the WLTP cycle. Consequently, lower electrical power is required from the battery to meet the same traction demand, leading to reduced energy consumption and increased vehicle range.

Furthermore, the slightly smaller benefit of regenerative braking observed for M2 suggests that its lower generator-mode efficiency at higher speeds limits the amount of recoverable energy during deceleration events. These findings highlight the importance of matching PMSM rotor topology to realistic driving-cycle operating conditions, rather than optimizing motor design solely for peak efficiency or high-speed performance.

Overall, the results indicate that BEV driving range is primarily governed by traction efficiency in the most frequently visited operating regions, while regenerative braking provides a secondary but significant contribution. The proposed methodology therefore offers a consistent basis for selecting PMSM rotor architectures according to the intended vehicle usage profile rather than peak-performance criteria alone.

While the present analysis focuses on the influence of rotor topology on vehicle-level energy performance, certain modeling simplifications should be acknowledged. Simplified inverter and battery representations may introduce deviations under highly dynamic load conditions or extreme thermal states. However, as both motor configurations are evaluated under identical modeling assumptions, the comparative conclusions remain unaffected.

Although the present study focuses on the impact of rotor topology on vehicle-level energy efficiency and driving range, other important industrial selection criteria such as manufacturing cost, thermal management, and long-term durability must also be considered. In the current analysis, both motor variants are evaluated under identical electrical, geometric, and thermal boundary conditions to isolate the influence of the electromagnetic design. Consequently, aspects such as detailed thermal management strategies, thermo-mechanical stresses, and lifecycle durability of the rotor structures are not explicitly modeled. Similarly, while differences in permanent-magnet material usage may have implications for manufacturing cost and supply-chain considerations, a comprehensive techno-economic assessment is beyond the scope of this work. These aspects represent important directions for future research, where multi-objective optimization frameworks integrating energetic, economic, and thermo-mechanical criteria could provide a more complete industrial evaluation of the proposed motor configurations.

Although the present study is limited to the WLTP Class 3 cycle, which represents moderate and standardized driving conditions, the operating-point distribution under more aggressive or sustained high-speed scenarios may differ significantly. Such conditions

could modify the relative efficiency performance of the motor topologies investigated. The proposed framework, however, is cycle-independent and can be directly applied to alternative driving profiles to evaluate topology robustness under diverse operating regimes.

5. Conclusions

This paper investigated the energy performance of two permanent magnet synchronous motor (PMSM) traction topologies for battery electric vehicles using a unified WLTP-based energy evaluation framework. The analysis combined FEM-derived motor efficiency maps with a longitudinal vehicle model, inverter loss modeling, battery constraints, and regenerative braking to assess the impact of rotor topology on real-world energy consumption and driving range.

- Even relatively small differences in the efficiency distribution of the traction motor led to measurable variations in battery energy demand and driving range over a complete WLTP driving cycle, despite the two PMSM variants exhibiting comparable peak efficiency and similar regenerative braking capability.
- The dominant operating regions imposed by the WLTP cycle play a decisive role in determining overall energy performance. Although both machines achieve high efficiency under specific conditions, their efficiency islands are differently aligned with the WLTP operating point distribution.
- The M1 configuration is better suited for urban and mixed driving conditions, as it maintains higher and more stable efficiency at low to medium speeds and moderate torque levels. Consequently, M1 consistently requires lower electrical power from the battery, exhibits reduced internal losses, and results in a lower RMS battery current over the cycle.
- The M2 configuration, while offering reduced permanent magnet material usage and extended high-speed field-weakening capability, does not fully exploit these advantages under WLTP conditions. The operating regimes where M2 performs most efficiently are only weakly represented in the cycle, leading to higher net energy consumption and a reduced driving range compared to M1.
- These findings highlight the importance of aligning traction motor design choices with the actual distribution of operating points dictated by the intended driving profile, rather than relying solely on peak efficiency or high-speed performance indicators.
- From a powertrain design perspective, reducing the amount of permanent magnet material does not automatically result in improved energy efficiency or extended driving range. A holistic evaluation that accounts for vehicle dynamics, control strategy, and real-world operating conditions is required to achieve balanced system-level performance.

The proposed methodology provides a robust and transferable framework for the early-stage comparison of traction motor topologies in battery electric vehicles, supporting informed design decisions that balance efficiency, material usage, and system-level performance. Future work will extend the present analysis to alternative driving cycles and control strategies. Overall, the results indicate that, under WLTP-dominant operating conditions, traction efficiency governs the achievable energy performance and driving range of a BEV, whereas marginal improvements in regenerative braking efficiency play a secondary role.

Author Contributions: Conceptualization, E.-D.L. and Ș.L.T.; methodology, E.-D.L. and Ș.L.T.; software, E.-D.L.; validation, E.-D.L. and Ș.L.T.; formal analysis, E.-D.L.; investigation, E.-D.L.; resources, E.-D.L.; data curation, E.-D.L.; writing—original draft preparation, E.-D.L.; writing—review and editing, E.-D.L. and Ș.L.T.; visualization, E.-D.L. and Ș.L.T.; supervision, Ș.L.T.; project

administration, E.-D.L. and Ș.L.T. All authors have read and agreed to the published version of the manuscript.

Funding: This research received no external funding.

Data Availability Statement: The original contributions presented in this study are included in the article. Further inquiries can be directed to the corresponding author.

Conflicts of Interest: The authors declare no conflicts of interest.

References

1. Alanazi, F. Electric Vehicles: Benefits, Challenges, and Potential Solutions for Widespread Adaptation. *Appl. Sci.* **2023**, *13*, 6016. [CrossRef]
2. DESTEC, M.C.; Lutzemberger, G.; Pasini, G.; Quilici, F.G.; Scarpelli, C.; Fioriti, D. Battery Electric Vehicles (BEV): More Efficient Than Expected? In Proceedings of the 2025 IEEE International Conference on Environment and Electrical Engineering and 2025 IEEE Industrial and Commercial Power Systems Europe (EEEIC/I&CPS Europe), Chania, Crete, Greece, 15–18 July 2025; pp. 1–6.
3. Miri, I.; Fotouhi, A.; Ewin, N. Electric vehicle energy consumption modelling and estimation—A case study. *Int. J. Energy Res.* **2021**, *45*, 501–520. [CrossRef]
4. Tabacu, S.; Popa, D. Backward-facing analysis for the preliminary estimation of the vehicle fuel consumption. *Sustainability* **2023**, *15*, 5344. [CrossRef]
5. Chavan, S.; Yeolekar, S.; Lokhande, N. Electric Vehicle Energy Consumption Modeling and Range Estimation using Different Topographical Drive Cycles. In Proceedings of the 2024 International Conference on Intelligent Systems and Advanced Applications (ICISAA), Pune, India, 25–26 October 2024; pp. 1–6.
6. Zhou, B.; Li, Z.; Wang, H.; Cui, Y.; Hu, J.; Jiang, F. Design and Optimization of an Electric Vehicle Powertrain Based on an Electromechanical Efficiency Analysis. *Processes* **2025**, *13*, 1698. [CrossRef]
7. Masri, J.; Ismail, M.; Obaid, A. Power Flow Simulation and Thermal Performance Analysis of Electric Vehicles Under Standard Driving Cycles. *Energies* **2025**, *18*, 3737. [CrossRef]
8. Wu, S.; Zhou, J.; Zhang, X.; Yu, J. Design and Research on High Power Density Motor of Integrated Motor Drive System for Electric Vehicles. *Energies* **2022**, *15*, 3542. [CrossRef]
9. Makaramani, M.; Wongyao, N.; Ruangjirakit, K. Simulation-based Comparative Study of EV Energy Consumption and Effects on the Lithium-ion Battery Aging under Different Driving Cycles. In Proceedings of the 2023 IEEE Transportation Electrification Conference and Expo, Asia-Pacific (ITEC Asia-Pacific), Chiang Mai, Thailand, 28 November–1 December 2023; pp. 1–8.
10. Kondru, J.; Obulesu, Y. Comprehensive performance analysis of an electric vehicle using multi-mode Indian drive cycles. *Sci. Rep.* **2025**, *15*, 17699. [CrossRef] [PubMed]
11. Kuttey, V.K.; Bali, S.K. Effect of Various Drive Cycles on Battery Electric Vehicle (BEV). In Proceedings of the 2024 International Conference on Computational Intelligence for Green and Sustainable Technologies (ICCIGST), Vijayawada, India, 18–19 July 2024; pp. 1–4.
12. Nucă, I.; Turcanu, A.; Cazac, V. Performance Analysis of an Urban Passenger Vehicle Powertrain Operating in Various Driving Cycle and Speed Profiles Using MatLab Simscape Models. In Proceedings of the 2023 International Conference on Electromechanical and Energy Systems (SIELMEN), Craiova, Romania, 12–13 October 2023; pp. 1–6.
13. Ibrahim, M.; Järg, O.; Seppago, R.; Rassõlkin, A. Performance Optimization of a High-Speed Permanent Magnet Synchronous Motor Drive System for Formula Electric Vehicle Application. *Sensors* **2025**, *25*, 3156. [CrossRef]
14. Bianchi, N.; Cinti, L.; Contò, C.; Ortombina, L. SPM Motor with Star-Delta Winding: Fault Analysis and Experimental Validation. *IEEE Trans. Ind. Appl.* **2024**, *61*, 47–55. [CrossRef]
15. Prajapati, A.M.; Prajapati, A.R.; Mehta, D.M. Advanced Control Strategies of PMSM for Battery Electric Vehicle Application: A Review. *J. Electr. Syst.* **2024**, *20*, 1139–1149. [CrossRef]
16. Shao, L.; Tavernini, D.; Karci, A.; Sorniotti, A. Design and optimisation of energy-efficient PM-assisted synchronous reluctance machines for electric vehicles. *IET Electr. Power Appl.* **2023**, *17*, 10. [CrossRef]
17. Jani, S.; Jamnani, J. Performance Validation of PM-Assisted SynRM and PMSM with Optimized Design for EV Application. *Trans. Energy Syst. Eng. Appl.* **2023**, *4*, 1–14. [CrossRef]
18. Park, G.-H.; Kim, J.-H.; Kim, J.-H.; Cha, K.-S.; Jung, Y.-H. Performance Comparison Between IPMSMs with Rare-Earth PM and Rare-Earth-Free PM According to Driving Cycle of Electric Vehicles. In Proceedings of the IEEE Energy Conversion Conference Congress and Exposition (ECCE), Philadelphia, PA, USA, 19–23 October 2025; pp. 1–7.
19. Cinti, L.; Carlet, P.G.; Ortombina, L.; Bianchi, N. Impact of Rotor Excitation Current During Flux-Weakening Control of Hybrid-Excited Permanent Magnet Synchronous Motor. *IEEE Trans. Ind. Appl.* **2024**, *61*, 313–321. [CrossRef]

20. Filippini, F.; Bianchi, N. Design of an On-Axis Electrically Excited Synchronous Motor for Heavy Commercial Vehicles. In Proceedings of the IEEE Energy Conversion Congress and Exposition (ECCE), Phoenix, AZ, USA, 20–24 October 2024; pp. 5185–5192.
21. Tupsaminder, P.B.; Mohite, H.; Jokare, M.; Shinde, R.; Mallad, H. Efficiency Map Model for PMSM to Use in EV Simulation. *Int. J. Sci. Res. Eng. Manag.* **2024**, *8*, 1–7. [CrossRef]
22. Contò, C.; Bianchi, N. E-Bike Motor Design Based on Analytical and Finite Element Performance Mapping. *IEEE Trans. Ind. Appl.* **2024**, *61*, 3854–3861. [CrossRef]
23. Di Leonardo, L.; Carbonieri, M.; Bianchi, N.; Tursini, M. Fast Mapping Procedure for Synchronous Reluctance Motors via Magnetic Coenergy Reconstruction Method from Boundaries Dataset. *IEEE Trans. Ind. Appl.* **2025**, *61*, 6160–6171. [CrossRef]
24. UNECE. Worldwide Harmonized Light Vehicles Test Procedure (WLTP). Available online: https://unece.org/transport/road-transport/working-party-automatedautonomous-and-connected-vehicles-introduction (accessed on 5 July 2025).
25. Zhao, X.; Ye, Y.; Ma, J.; Shi, P.; Chen, H. Construction of Electric Vehicle Driving Cycle for Studying Electric Vehicle Energy Consumption and Equivalent Emissions. *Environ. Sci. Pollut. Res.* **2020**, *27*, 37395–37409. [CrossRef]
26. Valladolid, J.; Calle, M.; Guiracocha, A. Analysis of regenerative braking efficiency in an electric vehicle through experimental tests. *Ingenius* **2023**, *29*, 24–31. [CrossRef]
27. Berjoza, D.; Pirs, V.; Jurgena, I. Research into the Regenerative Braking of an Electric Car in Urban Driving. *World Electr. Veh. J.* **2022**, *13*, 202. [CrossRef]
28. Anh, N.T.; Chen, C.-K.; Liu, X. An Efficient Regenerative Braking System for Electric Vehicles Based on a Fuzzy Control Strategy. *Vehicles* **2024**, *6*, 1496–1512. [CrossRef]
29. Li, C.; Zhang, L.; Lian, S.; Liu, M. Research on Regenerative Braking Control of Electric Vehicles Based on Game Theory Optimization. *Sci. Prog.* **2024**, *107*, 00368504241247404. [CrossRef]
30. Chidambaram, R.K.; Chatterjee, D.; Barman, B.; Das, P.P.; Taler, D.; Taler, J.; Sobota, T. Effect of Regenerative Braking on Battery Life. *Energies* **2023**, *16*, 5303. [CrossRef]
31. Gillespie, T.D. *Fundamentals of Vehicle Dynamics*; SAE International: Warrendale, PA, USA, 1992.
32. Ostadian, R.; Ramoul, J.; Biswas, A.; Emadi, A. Intelligent energy management systems for electrified vehicles: Current status, challenges, and emerging trends. *IEEE Open J. Veh. Technol.* **2020**, *1*, 279–295. [CrossRef]
33. Montaleza, C.; Arévalo, P.; Tostado-Véliz, M.; Jurado, F. Intrinsic Characteristics of Forward Simulation Modeling Electric Vehicle for Energy Analysis. *Electricity* **2022**, *3*, 202–219. [CrossRef]
34. Martyushev, N.V.; Malozyomov, B.V.; Sorokova, S.N.; Efremenkov, E.A.; Qi, M. Mathematical Modeling the Performance of an Electric Vehicle Considering Various Driving Cycles. *Mathematics* **2023**, *11*, 2586. [CrossRef]

Disclaimer/Publisher's Note: The statements, opinions and data contained in all publications are solely those of the individual author(s) and contributor(s) and not of MDPI and/or the editor(s). MDPI and/or the editor(s) disclaim responsibility for any injury to people or property resulting from any ideas, methods, instructions or products referred to in the content.